

Prediction of Turbulent Flow and Local Heat
Transfer in Internally Cooled Turbine Airfoils:
The Leading Edge Region

by

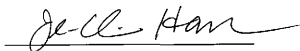
Juan Pablo Pontaza

Submitted to the Office of Honors Programs and Academic
Scholarships in partial fulfillment of the requirements for the
1998-99 University Undergraduate Research Fellows Program

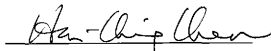
Texas A&M University

April 15, 1999

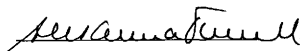
Approved as to style and content by:



Dr. J.C. Han
Mechanical Engineering Department



Dr. H.C. Chen
Civil Engineering Department



Dr. Susanna Finell
Honors Program and Academic Scholarships

Abstract

A multiblock numerical method has been employed for the calculation of three-dimensional flow and heat transfer in the leading edge of a large-scale impingement-cooled turbine airfoil. The finite-analytic method solves the Reynolds-Averaged Naviers-Stokes equations and the energy equation in conjunction with a two-layer k - ϵ isotropic eddy viscosity model and a near-wall Reynolds-Stress closure model. The fundamental cases of fully developed turbulent pipe flow and an axisymmetric jet impinging on a flat plate are also computed and compared with experimental data to assess the two turbulence models. Comparison of the two-layer model and the Reynolds-Stress model calculations clearly shows the anisotropic behavior of turbulence resulting from impingement. The predicted flow field showed flow separation and recirculation after impingement on the leading edge region. The predicted local heat transfer distribution on the leading edge of the turbine blade shows a maximum near the stagnation region with a gradual decrease in Nusselt number in the spanwise direction.

Acknowledgements

I would like to express my gratitude and appreciation to Dr. J.C. Han and Dr. H.C. Chen for their continued support, guidance, and encouragement throughout this year of research at Texas A&M University.

All computations were performed on the CRAY J90 at the Texas A&M Supercomputer Facility under a supercomputer research grant. Their support is greatly appreciated.

Contents

Nomenclature	ix
1 Introduction	1
1.1 Gas Turbine Blade Cooling	1
1.2 Numerical Predictions	4
1.3 Project Scope and Objectives	4
2 Governing Equations	7
2.1 Two-Layer k - ϵ model	8
2.2 Second-Moment Closure Model	11
3 The numerical method	16
3.1 Partial Transformation	16
3.2 The Finite-Analytic Method	18
3.3 General Solution Procedure	19

4	Grid Generation	21
4.1	Multi-Block or Composite Structured Grids	22
4.2	Composite Overset Structured Grids: Chimera	22
5	Fully developed turbulent pipe flow	25
5.1	Geometry and Grid Generation	25
5.2	Results and Discussion	26
6	Axisymmetric jet impinging on a flat plate	34
6.1	Geometry and Grid Generation	34
6.2	Results and Discussion	37
6.2.1	Aerodynamics of impinging jets	37
6.2.2	Heat Transfer	48
7	Impinging jet on the leading edge of a turbine blade	51
7.1	Geometry and Grid Generation	51
7.2	Results and Discussion	56
7.2.1	Turbulent flow field analysis	56
7.2.2	Heat Transfer	66
8	Conclusions and Recommendations	70
8.1	Conclusions	70
8.2	Recommendations	71

References	73
A Derivation of the RANS equations	75
B Derivation of the Reynolds Stress Tensor Transport equation	77
Biographical Sketch	81

List of Figures

1.1	Internal and external cooling in a typical gas turbine blade	2
4.1	Example of an overset grid	24
4.2	Overset grid after point removal and donor identification	24
5.1	Flow geometry and coordinate system	25
5.2	Axial mean velocity profile in wall coordinates ($Re_D = 23000$)	27
5.3	r.m.s. of the velocity fluctuations normalized by frictional velocity as a function of the distance from the centerline ($Re_D = 23000$)	30
5.4	Numerical and experimental data for the streamwise fluctuating velocities ($Re_D = 23000$)	31
5.5	Reynolds shear stress normalized by the shear stress at the wall as a function of the distance from the centerline ($Re_D = 23000$)	32
5.6	Axial mean velocity normalized by mean velocity ($Re_D = 23000$)	33
6.1	Geometry and computational domain	35
6.2	O-type grid around the pipe wall	36
6.3	Mass and momentum entrainment shown by velocity vectors	40

6.4	Normalized pressure contours at the stagnation region for $H/D = 2$ and $Re_D = 23,000$	41
6.5	Normalized velocity magnitude contours at the stagnation region and wall jet region for $H/D = 2$ and $Re_D = 23,000$	42
6.6	Normalized turbulent kinetic energy contours by two-layer model for $H/D = 6$ and $Re_D = 23,000$	43
6.7	Normalized turbulent kinetic energy contours by Reynolds-Stress model for $H/D = 6$ and $Re_D = 23,000$	44
6.8	Radial velocity fluctuations squared ($\overline{u_r^2}$) by Reynolds-Stress model for $H/D = 6$ and $Re_D = 23,000$	45
6.9	Axial velocity fluctuations squared ($\overline{u_y^2}$) by Reynolds-Stress model for $H/D = 6$ and $Re_D = 23,000$	46
6.10	Circumferential velocity fluctuations squared ($\overline{u_\theta^2}$) by Reynolds-Stress model for $H/D = 6$ and $Re_D = 23,000$	47
6.11	Nusselt number distribution for $H/D = 6$ and $Re_D = 23,000$	50
7.1	Top view of the computational domain	52
7.2	Three-dimensional geometry and coordinate system	53
7.3	Plenum-hole-airfoil Chimera intersection	54
7.4	Plenum-hole-airfoil fully connected intersection	55
7.5	Normalized velocity magnitude contours on the spanwise symmetry plane for $Re_D = 25,000$	59
7.6	Normalized pressure contours on the spanwise symmetry plane for $Re_D = 25,000$	60

7.7	Velocity vector field showing the recirculation region on the spanwise symmetry plane for $Re_D = 25,000$	61
7.8	Turbulent kinetic energy contours on the spanwise symmetry plane for $Re_D = 25,000$	62
7.9	Velocity vector field in the spanwise symmetry plane colored by axial (z) velocity for $Re_D = 25,000$	63
7.10	Normalized velocity vector field in the chordwise symmetry plane for $Re_D = 25,000$	64
7.11	Normalized velocity magnitude contours on the chordwise symmetry plane for $Re_D = 25,000$	65
7.12	Normalized temperature contours on the spanwise symmetry plane for $Re_D = 25,000$	67
7.13	Normalized temperature contours on the chordwise symmetry plane for $Re_D = 25,000$	68
7.14	Local nusselt number distribution on the leading edge of the airfoil for $Re_D = 25,000$ and $z/D = 3.04$	69

Nomenclature

c_p	specific heat
D	diameter
e_{ijk}	third rank permutation tensor
g^{ij}	metric tensor
h	convective heat transfer coefficient
J	Jacobian
K	thermal conductivity
k	turbulent kinetic energy
l	turbulent length scale
Nu_D	Nusselt number, $Nu_D = hD/K$
p	pressure
Pr	Prandtl number
q	heat flux
R^{ij}	Reynolds Stress Tensor, $R^{ij} = \overline{u^i u^j}$
Re_D	Reynolds number, $Re_D = \rho U D / \mu$
T	temperature
U^i	mean contravariant velocity component
u^i	fluctuating contravariant velocity component

Greek Symbols

Ω	rotational speed
ϵ	dissipation rate of turbulence
μ	dynamic viscosity
ν	kinematic viscosity
ν_t	eddy viscosity
ρ	density
ξ^i	contravariant coordinate component

Subscripts

i, j, k, \dots	covariant components
$, i$	covariant derivative with respect to ξ^i

Superscripts

i, j, k, \dots	contravariant components
$-$	ensemble average
$'$	fluctuating component
$+$	in 'wall coordinates'
$*$	dimensionless

Chapter 1

Introduction

1.1 Gas Turbine Blade Cooling

Turbine inlet temperatures over the next few years will approach $1650^{\circ}C$ ($3000^{\circ}F$) at maximum power for the largest commercial turbofan engines, resulting in high fuel efficiency and thrust levels approaching 445 kN (1,000 lbs). High reliability and durability must be designed into these turbine engines to meet operating economic targets and certification requirements. This level of performance has been brought about by a combination of advances in air cooling for turbine blades and vanes, and the development of single crystal and directionally solidified casting processes.

The evolution of the gas turbine engine has continually required the combined advances of several engineering fields. The most important of these fields has been, and continues to be heat transfer. Heat transfer considerations play an important role with respect to various components in the engine. Accurate heat transfer analyses are required to predict component dimensions and relative positioning under the influence of thermal stresses superimposed on top of centrifugal stresses. These predictions

must be carried out over a variety of operating conditions, both transient and steady state.

The use of various cooling schemes in gas turbine airfoils has been investigated to ascertain more effective ways of providing cooling. A typical airfoil may utilize both jet impingement cooling and film cooling in the leading edge region, while the midchord and trailing edge regions may be convection cooled with augmentation via roughness elements and pin fins. All these cooling schemes are forms of convective heat transfer which involve turbulent, three-dimensional flows in highly complex geometries. Figure 1.1 shows the typical cooling schemes in an advanced gas turbine airfoil.

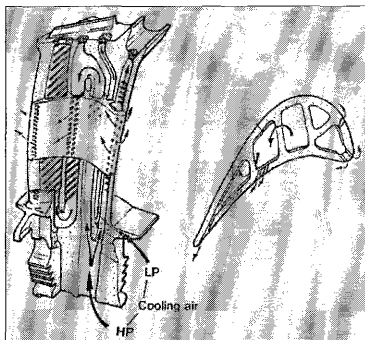


Figure 1.1: Internal and external cooling in a typical gas turbine blade

The airfoil leading edge region, as shown in Figure 1.1, involves jet impingement and film cooling. Heat transfer in such a geometry is necessarily dependent upon the

interacting effects of many variables. The parameters which may affect the flow and heat transfer are many. These include:

- Prandtl number
- Reynolds number based on jet diameter
- Radius of curvature of the the leading edge
- Spacing of the leading edge from jet nozzle
- Film cooling hole distribution
- Film cooling hole angle

In addition to all of these parameters is the difficulty of dealing with an airfoil which is typically rotating at about 9000 rpm.

The possible effects of these parameters just mentioned are compounded by their interaction. The beneficial effect of a given jet size and distribution may be offset by the leading edge sharpness or the film cooling hole angle and locations. Certain parameters may be limited in range due to other design considerations. For example; the leading edge sharpness may be dictated by the external aerodynamic design of the airfoil.

The prediction of airfoil surface temperature, heat transfer convective coefficients, and three dimensional turbulent flow is necessary in order to improve the cooling schemes in gas turbine airfoils. Five years ago, experimental methods were the only means to obtain detailed and reliable convective heat transfer information in the complex cooling flow. At present, with the advances in CPU speed and memory size, super computers are able to numerically solve the differential equations governing

fluid flow and heat transfer over complex geometries in a relatively short period of time.

1.2 Numerical Predictions

Numerical solutions of the complete Navier-Stokes equations for laminar flow and the Reynolds-Averaged equations for turbulent flow have received a great deal of attention in recent years since, in principle, they describe flows with any level of complexity, the only uncertainty being that introduced by the turbulence model employed to effect closure of the Reynolds stress tensor equation. As available computing power increases, many problems of practical interest, which invariably involve complex three-dimensional geometries, are becoming feasible to solve through solutions of the complete equations. The progress being made in numerical generation of computational grids for arbitrary curvilinear geometries greatly facilitate such applications.

Computational Fluid Dynamics (CFD) is beginning to play a major role in the analysis and design of turbomachinery. A new era is dawning in the ability to predict turbulent flow and convection heat transfer in the turbine gas path. Historically, experimental work and the modeling of the physics have preceded the complex computational predictions of the phenomena. This is particularly true with respect to heat transfer.

1.3 Project Scope and Objectives

The present study is concerned with the implementation of a numerical method for the solution of the Reynolds-Averaged Navier-Stokes equations based on partial transformation of the governing equations. For complete generality, the equations are writ-

ten in non-orthogonal curvilinear coordinates. Closure of the Reynolds stress tensor equation is effected by an isotropic two-layer k - ϵ turbulence model and an anisotropic Reynolds stress closure model. The transport equations of momentum and turbulence parameters are discretized using the finite-analytic method of Chen and Chen [1]. Pressure velocity coupling is established via the continuity equation by a modified version of the SIMPLER algorithm of Patankar [2].

The research has as its main objective the determination of turbulent flow and local heat transfer coefficients in the leading edge region of an airfoil which utilizes impingement cooling.

Specifically, the computational programme followed over the course of the research may be outlined as follows:

- **Pre-Processing**

1. Multiblock Grid Generation
2. Grid Reblocking
3. Generation of Composite Grid by Chimera Method

- **Two-Layer k - ϵ model**

1. Turbulent pipe flow computation
2. Axisymmetric turbulent jet impinging on a flat plate computation
3. Three-Dimensional turbulent jet impinging on the leading edge of a gas turbine airfoil computation

- **Reynolds-Stress model**

1. Turbulent pipe flow computation

2. Axisymmetric turbulent jet impinging on a flat plate computation

• **Post-Processing**

1. Investigate the anisotropic behavior of turbulence in fully developed pipe flow and in the impinging jet problem
2. Assess the isotropic and nonisotropic models by comparing with experimental data
3. Understand and interpret the highly three-dimensional flow field in the leading edge of the turbine airfoil

As can be seen from the computational programme, this research is also concerned with the computation of turbulent pipe flow and the famous axisymmetric impinging jet on a flat plate problem. These computations were necessary in order to assess the turbulence models and capture the physics of the impinging jet problem in a simple geometry.

Chapter 2

Governing Equations

In the present study, calculations were performed for a fully developed pipe flow, a jet impinging on a flat plate, and a jet impinging on the leading edge region of a turbine blade. The two-layer eddy viscosity model of Chen and Patel [3] and the near-wall second-order Reynolds stress closure model of Chen [4, 5] were used for the computations. Both models were developed originally for incompressible flows in non-rotating coordinates. They have been generalized here to include the effects of rotation.

Consider the Reynolds-Averaged Navier-Stokes equations in general curvilinear coordinates (ξ^i, t) , $i = 1, 2, 3$ for unsteady incompressible flow:

$$\frac{\partial \rho}{\partial t} + (\rho U^m)_{,m} = 0 \quad (2.1)$$

$$\rho \left(\frac{\partial U^i}{\partial t} + U^m U_{,m}^i + R_{,m}^{im} \right) + 2\rho g^{il} e_{imn} \Omega^m U^n + \rho g_{mn} (\Omega^i \Omega^m \xi^n - \Omega^m \Omega^n \xi^i) = -g^{im} p_{,m} + (\mu g^{mn} U_{,n}^i)_{,m} \quad (2.2)$$

where e_{lmn} is the third rank permutation tensor, Ω^m is the coordinate rotation vector, g_{mn} is the metric tensor, and g^{mn} the conjugate metric tensor. $R^{im} = \overline{u^i u^m}$ is the Reynolds stress tensor where overbars imply the ensemble Reynolds averaging and the summation convention is used for repeated indices. The subscript , m represents the covariant derivative with respect to ξ^m . U^i and u^i are contravariant components of the mean and fluctuating velocities, t is time and p is pressure.

The energy equation is also solved to obtain the temperature field and the convective heat transfer coefficients:

$$\rho c_p \left(\frac{\partial T}{\partial t} + U^m T_{,m} + \overline{u^m T'} \right) = g^{mn} (KT_{,n})_{,m} + \frac{Dp}{Dt} + \Phi \quad (2.3)$$

and Φ is the dissipation function defined by

$$\Phi = -\mu \left[U_{,n}^m U_{,m}^n + \overline{u_{,n}^m u_{,m}^n} + g_{ij} g^{mn} \left(U_{,m}^i U_{,n}^j + \overline{u_{,m}^i u_{,n}^j} \right) \right] \quad (2.4)$$

where T and T' are the mean and fluctuating temperature fields, c_p is the specific heat at constant pressure, K is the thermal conductivity, and $\overline{u^m T'}$ is the kinematic turbulent heat flux. A complete and detailed derivation of the Reynolds-Averaged Navier-Stokes equations in general curvilinear coordinates is given in the appendix.

2.1 Two-Layer k - ϵ model

The two-layer model of Chen and Patel [3] is employed to provide closure for the Reynolds stress tensor R^{ij} . In this approach, the Reynolds stresses are related to the corresponding mean rate of strain through an isotropic eddy viscosity, ν_t :

$$-R^{ij} = 2\nu_t S^{ij} - \frac{2}{3} g^{ij} k \quad (2.5)$$

where S^{ij} are the contravariant components of the mean rate of stress tensor:

$$S^{ij} = \frac{1}{2} \left(g^{jm} U_{,m}^i + g^{im} U_{,m}^j \right) \quad (2.6)$$

and k is the turbulent kinetic energy:

$$k = \frac{1}{2} g_{ij} \overline{u^i u^j} \quad (2.7)$$

Similarly, the turbulent heat fluxes can be related to the mean temperature gradient as follows:

$$-\overline{u^m T^v} = \frac{\nu_t}{Pr_t} g^{mn} T_{,n} \quad (2.8)$$

where Pr_t is the turbulent Prandtl number. Substitution into (2.2) and (2.3) yields momentum and energy equations for eddy viscosity turbulence modeling:

$$\begin{aligned} \frac{\partial U^i}{\partial t} + U^m U_{,m}^i + g_{mn} \left(\Omega^i \Omega^m \xi^n - \Omega^m \Omega^n \xi^i \right) + g^d e_{lmn} \Omega^m U^n = \\ - g^{im} \left(\frac{p}{\rho} + \frac{2}{3} k \right)_{,m} + 2\nu_{t,m} S^{im} + (\nu + \nu_t) g^{mn} U_{,mn}^i \end{aligned} \quad (2.9)$$

$$\frac{\partial T}{\partial t} + U^m T_{,m} = g^{mn} \left[\left(\frac{\nu}{Pr} + \frac{\nu_t}{Pr_t} \right) T_{,n} \right]_{,m} \quad (2.10)$$

where Pr are the Prandtl numbers. Equations (2.9) and (2.10) are closed using the two-layer turbulence model of Chen and Patel [3]. The approach utilizes a two-equation k - ϵ model for most of the flow field, but a one-equation k - l model in the

viscous sublayer and buffer layer. The prescribed length scale (l) circumvents numerical problems often encountered with near-wall dissipation calculations, and results in a more realistic sublayer profile.

In the fully turbulent region, the conservation equations for turbulent kinetic energy and its dissipation rate can be written:

$$\frac{\partial k}{\partial t} + U^m k_{,m} = g^{mn} \left[\left(\nu + \frac{\nu_t}{\sigma_k} \right) k_{,n} \right]_{,m} + P - \epsilon \quad (2.11)$$

$$\frac{\partial \epsilon}{\partial t} + U^m \epsilon_{,m} = g^{mn} \left[\left(\nu + \frac{\nu_t}{\sigma_\epsilon} \right) \epsilon_{,n} \right]_{,m} + \frac{\epsilon}{k} (C_{\epsilon 1} P - C_{\epsilon 2} \epsilon) \quad (2.12)$$

where the production term P is given by:

$$P = 2g_{np} \nu_t S^{mn} U_{,m}^p \quad (2.13)$$

and the eddy viscosity is computed from:

$$\nu_t = C_\mu \frac{k^2}{\epsilon} \quad (2.14)$$

the model coefficients ($C_\mu, C_{\epsilon 1}, C_{\epsilon 2}, \sigma_k, \sigma_\epsilon$) are equal to (0.09, 1.44, 1.92, 1.0, 1.3).

In the near-wall region, the rate of turbulent dissipation is specified in terms of k rather than being computed from (2.12). From Chen and Patel [3]:

$$\epsilon = \frac{k^{3/2}}{l_\epsilon} \quad (2.15)$$

where l_ϵ is a dissipation length scale given by:

$$l_\epsilon = C_l y \left[1 - \exp\left(-\frac{R_y}{A_\epsilon}\right) \right] \quad (2.16)$$

with

$$R_y = \frac{\sqrt{k}y}{\nu} \quad (2.17)$$

With k and ϵ known, the eddy viscosity is found from:

$$\nu_t = C_\mu l_\mu \sqrt{k} \quad (2.18)$$

where

$$l_\mu = C_l y \left[1 - \exp\left(-\frac{R_y}{A_\mu}\right) \right] \quad (2.19)$$

The constants C_l , A_μ , and A_ϵ are chosen to yield a smooth distribution of eddy viscosity between the two regions, and take the values ($C_l = 0.418C_\mu^{-3/4}$, $A_\mu = 70$, $A_\epsilon = 2C_l$).

2.2 Second-Moment Closure Model

Consider the Reynolds stress tensor transport equation:

$$\frac{\partial R^{ij}}{\partial t} + C^{ij} = P^{ij} + D_v^{ij} + D_p^{ij} + \Phi^{ij} + D_\nu^{ij} - \epsilon^{ij} \quad (2.20)$$

Where

- C^{ij} : Convection

$$U^m R_{,m}^{ij}$$

- P^{ij} : Production

$$-\left(R^{im}U_{,m}^j + R^{jm}U_{,m}^i\right) - 2e_{lmn}\Omega^m\left(g^{il}R^{jn} + g^{jl}R^{in}\right)$$

- D_v^{ij} : Diffusion by Velocity Fluctuation

$$-\left(u^m u^i u^j\right)_{,m}$$

- D_p^{ij} : Diffusion by Pressure Fluctuation

$$-\frac{1}{\rho}g^{im}\left(\overline{u^j p'}\right)_{,m} - \frac{1}{\rho}g^{jm}\left(\overline{u^i p'}\right)_{,m}$$

- Φ^{ij} : Pressure-Strain

$$\frac{\overline{p'}}{\rho}\left(g^{im}\overline{u_{,m}^j} + g^{jm}\overline{u_{,m}^i}\right)$$

- D_ν^{ij} : Viscous Diffusion

$$\nu g^{mn}R_{,m,n}^{ij}$$

- ϵ^{ij} : Viscous Dissipation

$$2\nu g^{mn}\overline{u_{,m}^i u_{,n}^j}$$

To solve these equations, appropriate closure models must be provided for the pressure-strain, diffusion and dissipation terms. In the present study, the pressure-strain correlation of Speziale, Sarkar, and Gatski [6] was combined with the near-wall Reynolds stress closure of Chen [4, 5] for detailed resolution of three-dimensional boundary layer flow all the way up to the solid walls. For the sake of completeness, a brief summary of the near-wall second-moment closure model is given:

1. **Diffusion** $D^{ij} = D_v^{ij} + D_p^{ij}$ (Daly and Harlow [7])

$$D^{ij} = C'_s \left(\frac{k}{\epsilon} R^{mn} R_{,n}^{ij} \right)_{,m} \quad (2.21)$$

2. **Pressure-Strain and Dissipation** $\Phi^{ij} - \epsilon^{ij}$ (Speziale, Sarkar, Gatski [6]; Chen [4, 5])

$$\Phi^{ij} - \epsilon^{ij} = \overline{\Phi}_1^{ij} + \Phi_2^{ij} + \Phi_w^{ij} - \frac{2}{3} g^{ij} \epsilon \quad (2.22)$$

where

$$\overline{\Phi}_1^{ij} = -\overline{C}_1 \left[1 - \left(1 - \frac{1}{\overline{C}_1} \right) f_w \right] \epsilon b^{ij} + C_2 (1 - f_w) \epsilon \left(g_{mn} b^{im} b^{jn} - \frac{1}{3} g^{ij} \Pi \right) \quad (2.23)$$

$$\begin{aligned} \Phi_2^{ij} = & \left(C_3 - C_3^* \Pi^{\frac{1}{2}} \right) k S^{ij} + C_4 k \left(g_{mn} b^{im} S^{jn} + g_{mn} b^{jm} S^{in} \right. \\ & \left. - \frac{2}{3} g^{ij} g_{mr} g_{ns} b^{mn} S^{rs} \right) + C_5 k \left(g_{mn} b^{im} W^{jn} + g_{mn} b^{jm} W^{in} \right) \end{aligned} \quad (2.24)$$

$$\Phi_w^{ij} = f_w \left[0.45 \left(P^{ij} - \frac{2}{3} g^{ij} P \right) - 0.03 \left(Q^{ij} - \frac{2}{3} g^{ij} P \right) + 0.08 k \left(2S^{ij} \right) \right] \quad (2.25)$$

and

$$b^{ij} = \frac{R^{ij}}{2k} - \frac{1}{3} g^{ij} \quad (2.26)$$

$$\Pi = g_{mr} g_{ns} b^{mn} b^{rs} \quad (2.27)$$

$$W^{ij} = \frac{1}{2} (g^{jm} U_{,m}^i - g^{im} U_{,m}^j) \quad (2.28)$$

$$P = \frac{1}{2} g_{mn} P^{mn} \quad (2.29)$$

$$Q^{ij} = -g_{lm} (g^{in} R^{jl} + g^{jn} R^{il}) U_{,n}^m \quad (2.30)$$

$$\overline{C_1} = C_1 + C_1^* \frac{P}{\epsilon} \quad (2.31)$$

$$f_w = \exp \left[- \left(0.0184 Re \sqrt{k} y \right)^4 \right] \quad (2.32)$$

where the model coefficients (C_1 , C_1^* , C_2 , C_3 , C_3^* , C_4 , C_5) are equal to (3.4, 1.80, 4.2, 0.8, 1.30, 1.25, 0.40) respectively. It should be remarked that the coefficient in f_w was adjusted from 0.015 to 0.0184 based on numerical optimizations for the present test cases.

It is important to note that the effects of the damping function f_w diminish exponentially away from the solid surfaces with $\Phi_w^{ij} = 0$ in the fully developed turbulent regions. Therefore, the present near-wall Reynolds stress model automatically recovers the the high-Re SSG second-moment closure of Speziale, Sarkar, and Garski [6] in the far field. A more detailed description of the present near-wall second-moment closure is given in Chen [4, 5].

In general, the turbulent heat fluxes $\overline{u^m T^v}$ may also be solved directly using second-order models such as those shown in Launder [10]. In the present study, however, a generalized gradient diffusion hypothesis (GGDH) was used:

$$\overline{u^m T'} = -C_\theta \frac{k}{\epsilon} R^{mn} T_{,n} \quad (2.33)$$

with $C_\theta = 0.225$.

To complete the Reynolds stress closure, the rate of turbulent kinetic energy dissipation ϵ must also be modeled. In the present study, the low Reynolds number model of Shima [8] was adopted with minor modifications as follows:

$$\frac{\partial \epsilon}{\partial t} + U^m \epsilon_{,m} = \left[\left(\nu g^{mn} + C_\epsilon \frac{k}{\epsilon} R^{mn} \right) \epsilon_{,n} \right]_{,m} + C_{\epsilon 1} (1 + C_{\epsilon 3} f_w) \frac{\epsilon}{k} P - C_{\epsilon 2} f_\epsilon \frac{\epsilon \epsilon^*}{k} \quad (2.34)$$

where

$$f_\epsilon = 1 - \frac{2}{9} \exp \left[- \left(\frac{R_T}{6} \right)^2 \right] \quad (2.35)$$

$$R_T = \frac{k^2}{\nu \epsilon} \quad (2.36)$$

The near-wall damping function f_w is given earlier and the model coefficients are $(C_\epsilon, C_{\epsilon 1}, C_{\epsilon 2}, C_{\epsilon 3}) = (0.15, 1.35, 1.8, 1.0)$.

Chapter 3

The numerical method

3.1 Partial Transformation

For three-dimensional flows involving complex geometries, it is desirable to employ body-fitted coordinate systems so that the flow in the wall layer can be accurately resolved with a reasonable number of grid points. Once such a coordinate system is selected for a given geometry, there remains the task of formulating the equations of motion in that system. Two different approaches can be adopted for this purpose. One of them is the so called “partial transformation”, in which only the independent coordinate variables are transformed, leaving the dependent variables (i.e. velocity components) in a preselected orthogonal coordinate system. This approach, which was the one used in the present study, has the advantage that the resulting equations have a strong conservation form and facilitate the use of pressure-velocity coupling algorithms based on conservation of mass. Also, the equations are relatively simple and the results can be readily interpreted. Since the velocity vectors, in general, do not align with the coordinate directions, this approach may lead to increased numerical

diffusion when the angles between the velocity components and coordinate surfaces become large. The alternative is to transform the governing equations completely, including the independent as well as the dependent variables. The use of contravariant velocity components in such a complete transformation allows a much more accurate resolution of the flow near a solid surface. However, the fully-transformed equations involve many more geometric coefficients and their higher order derivatives. This not only leads to increased computer storage requirements but also can adversely affect the flow solution if the coefficients are not smooth and accurate, especially the Christoffel symbols of the second kind which involve summations of higher order derivatives. In many practical applications it is not necessary to use the complete transformation if the basic coordinate systems are chosen carefully so as to avoid large skew angles between velocity components and the faces of the computational cell.

Using the partial transformation described in Chen, Patel, and Ju [9]; the continuity equations and the momentum equations become:

$$\frac{1}{J} \sum_{i=1}^3 \sum_{j=1}^3 \frac{\partial}{\partial \xi^i} [b^j U(j)] = 0 \quad (3.1)$$

$$\frac{\partial U(i)}{\partial t} + \sum_{j=1}^3 C_{U(i)}^j \frac{\partial U(i)}{\partial \xi^j} - \frac{1}{R_U} \nabla^2 U(i) + s_{U(i)} = 0 \quad (3.2)$$

and the transport equations for k and ϵ in the two layer model become:

$$\frac{\partial k}{\partial t} + \sum_{j=1}^3 C_k^j \frac{\partial k}{\partial \xi^j} - \frac{1}{R_k} \nabla^2 k + s_k = 0 \quad (3.3)$$

$$\frac{\partial \epsilon}{\partial t} + \sum_{j=1}^3 C_\epsilon^j \frac{\partial \epsilon}{\partial \xi^j} - \frac{1}{R_\epsilon} \nabla^2 \epsilon + s_\epsilon = 0 \quad (3.4)$$

The above transport equations for $U(i)$, k , ϵ , and also R^{ij} can be cast in the form of a general convection/diffusion equation:

$$\sum_{j=1}^3 \left(g^{ij} \frac{\partial^2 \phi}{\partial \xi^i \partial \xi^j} - a_\phi^j \frac{\partial \phi}{\partial \xi^j} \right) = R_\phi \frac{\partial \phi}{\partial t} + S_\phi \quad (3.5)$$

where ϕ is any transport quantity.

3.2 The Finite-Analytic Method

In the finite analytic approach, Equation 3.5 is linearized in each local element of dimensions $\Delta \xi^1 = \Delta \xi^2 = \Delta \xi^3 = 2$ and solved analytically by the method of separation of variables. Evaluation of the analytic solution at the interior node provides a stencil for the center point in terms of its nearest neighbors. Using Euler implicit differencing in time, and lumping streamwise influences into single points upstream and downstream, results in a 12-point discretization formula:

$$\phi_P = \frac{1}{1 + C_P (C_U + C_D + R_\phi / \Delta t)} \left[\sum_{m=1}^8 C_m \phi_m + C_P \left(C_U \phi_U + C_D \phi_D + \frac{R_\phi}{\Delta t} \phi_P^{n-1} \right) - C_P (S_\phi)_P \right] \quad (3.6)$$

where subscripts U and D represent points in the stencil upstream and downstream of P , and subscripts m ($m = 1, 8$) represent the eight nearest points to P in the cross-flow plane. Expressions for the finite-analytic coefficients (C_P , C_U , C_D , C_m) can be found in Chen, Patel, and Ju [9].

3.3 General Solution Procedure

The solution procedure consists of an outer loop over time and an inner loop or sweep that iterates over the blocks of the grid. The system of discretized equations generated for each block is solved using an iterative ADI scheme, resulting in a tridiagonal system of equations. For unsteady problems, the solution procedure can be summarized as follows:

1. Construct the grids for each component of the configuration.
2. Construct a boundary condition table specifying appropriate boundary conditions for each face.
3. Specify the initial conditions for velocity, pressure, and turbulence fields.
4. Determine interpolation information to link the grids using the *PEGSUS* program (discussed in the next chapter).
5. Calculate the geometric coefficients.
6. Calculate the finite-analytic coefficients and the source functions.
7. Solve the momentum equations and the turbulence equations using the iterative ADI scheme.
8. Calculate the pseudovelocities.
9. March to the next downstream station and repeat steps 6 through 8.
10. After reaching the last downstream station, solve the pressure equation. Several iterations *from downstream to upstream* are employed to update the three-dimensional elliptic pressure field. Depending upon the time step employed, some under-relaxation of pressure is required for convergence.

11. Repeat steps 6 through 10 for several sweeps until both the pressure and velocity fields have converged within a specific tolerance.
12. Return to step 6 for the next time step.

Chapter 4

Grid Generation

The grid generation process, in general, proceeds from first defining the boundary geometry. Then points are distributed on the curves that form the edge of boundary sections. A surface grid is then generated on the boundary surface, and finally a volume grid is generated in the field.

A mesh or volume grid is a set of points distributed over a calculation field for a numerical solution of a set of partial differential equations (PDEs), in this case, the Reynolds-Averaged Navier-Stokes equations. These set of points may be structured, e.g., formed by the intersections of curvilinear coordinate surfaces, or unstructured, i.e., with no relation to coordinate directions. The structured grid can be generated algebraically by interpolation from boundaries, e.g., transfinite interpolation (TFI), or by solving a set of partial differential equations in the region. In the present study, structured grids were used to represent the physical domains. *GRIDGEN*, an interactive multi-block grid generation software package, was used to generate the volume grids.

4.1 Multi-Block or Composite Structured Grids

Here, *multi-block* refers to the fact that the physical region is divided into sub-regions within each of which a structured grid is generated. These subgrids may be patched together at common interfaces, may be overlaid, or may be connected by an unstructured grid. Considerable confusion has arisen in regard to terminology for composite grids, making it difficult to immediately classify papers on the subject.

Composite grids in which the subgrids share common interfaces are referred to as *block*, *patched*, *embedded*, or *zonal grids* in literature. The use of the first two of these terms is fairly consistent with this type of grid, but the last two are sometimes also applied to overset grids. Overset grids are often called *Chimera* grids after the composite monster of Greek mythology. Unfortunately, the common interface grids can also be said to overlap, since they typically use surrounding layers of points to achieve continuity. Embedded grids can be almost anything, and the term is probably best avoided.

4.2 Composite Overset Structured Grids: Chimera

The multiblock *Chimera* method of domain decomposition was used to generate the composite grid for the turbine airfoil. In the *Chimera* approach, grid components are not required to align with neighboring components in any special way. Accordingly, the approach offers an additional degree of flexibility that is not available with a fully connected multiblock approach. Another novel contribution of *Chimera* to the overall approach of structured grid based domain decomposition is the allowance for **holes** within grid components.

The cost of the advantages inherent to an overset grid approach are reflected in

the need to establish domain connectivity. Domain connectivity is the communication of dependent variable information between grid components. Transmission of this information occurs through the intergrid boundary points by interpolation from the interior of overlapping neighboring grid systems. Accordingly, the domain connectivity solution for a given system of overlapping grids is the identity of a suitable donor element for each intergrid boundary point on the system.

General implementations of the method must allow for grid components posed in curvilinear coordinate systems. This fact makes the task of establishing domain connectivity nontrivial. The position of points within all grid components is defined relative to a fixed reference frame. Data structure is realized on a component-wise basis due to the fact that grid points are distributed along curvilinear coordinate lines. However, the coordinate systems of the respective grid components are mutually independent. Hence, there is no direct correspondance between the computational space of one grid component and that of any other component in the system. The task of establishing domain connectivity can be stated for a single intergrid boundary point as follows. Given an intergrid boundary point P , identify a grid component that can satisfy the domain connectivity needs of P , and the position of P within the computational space of the domain component.

PEGSUS, a code developed at Arnold Air Force Base, was used to generate the composite mesh and associated *Chimera* interpolation data for use in the flow solver. Figure 4.1 shows an example of an overset grid. The surface is actually part of the plenum-hole intersection of the turbine airfoil mesh. The overset grid consists of a cylindrical grid inside a cartesian-type grid. *PEGSUS* was used to remove unnecessary points from inside the cylindrical mesh and to find donor points to communicate the two grids. Figure 4.2 shows the same overset grid after hole cutting and donor point identification.

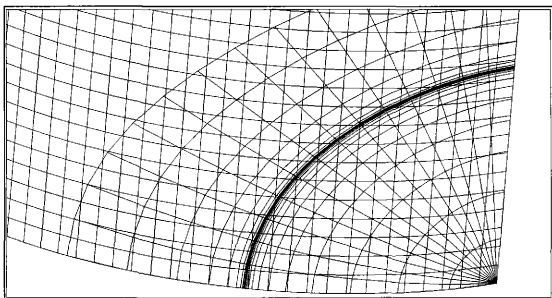


Figure 4.1: Example of an overset grid

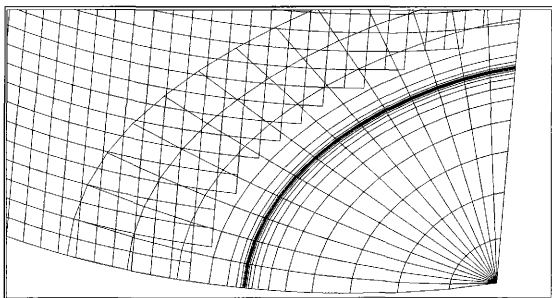


Figure 4.2: Overset grid after point removal and donor identification

Chapter 5

Fully developed turbulent pipe flow

5.1 Geometry and Grid Generation

The turbulent pipe flow was studied in the cylindrical geometry shown in Figure 5.1. The diameter of the pipe is denoted by D , and the length of the computational domain by L , with $L = 70D$. Such a large aspect ratio was required in order for the flow to become fully developed. The Reynolds number based on pipe diameter D and on mean velocity was equal to $Re_D = 23,000$.

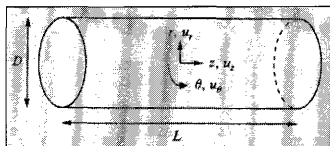


Figure 5.1: Flow geometry and coordinate system

From symmetry about the axis of the pipe, only three planes were required in the circumferential (θ) direction. The present computations were carried out with a $41 \times 210 \times 3$ non-uniform, orthogonal grid in the r , z , θ direction respectively. The minimum grid spacing in the near-wall region was maintained at 10^{-4} of the body length which corresponds to a wall coordinate y^+ of the order of 0.1. This enabled the computation of the viscous sublayer and buffer layer of the fully developed turbulent flow. It should be emphasized that commercial codes cannot handle such fine spacing near the wall and have to place their first point at $y^+ \approx 10$. Instead of computing the viscous sublayer and buffer layer, commercial codes use an analytic profile given by the universal law of the wall. This introduces error into the fully turbulent region and consequently into the entire computational domain, especially when there is flow separation or a negative pressure gradient.

5.2 Results and Discussion

The turbulent pipe flow was computed using the two-layer model and the Reynolds-Stress model. Laser Doppler Anemometry (LDA) and Particle Image Velocimetry (PIV) measurements made by Eggels et. al. [11] in 1994 are used to assess the turbulence models. Figure 5.2 shows the computed and measured mean velocity profiles in wall coordinates. The plot is semilogarithmic, where the following definitions apply:

$$u^+ = \frac{u}{u_\tau} \quad (5.1)$$

$$y^+ = Re \frac{y}{D} u_\tau \quad (5.2)$$

where u_τ is the frictional velocity, defined as:

$$u_r = \sqrt{\frac{\tau_w}{Re}} \quad (5.3)$$

and τ_w is the shear stress at the wall.

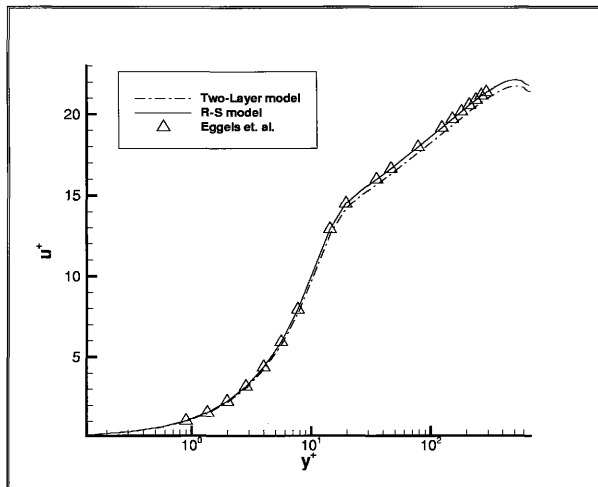


Figure 5.2: Axial mean velocity profile in wall coordinates ($Re_D = 23000$)

The entire law of the wall is divided into three regions, where of course, there is no sudden transition from one region to the next:

1. **viscous sublayer:** $0 \leq y^+ \leq 5$

2. **buffer layer:** $5 \leq y^+ \leq 30$

3. **logarithmic layer:** $y^+ \geq 30$

Both, the two-layer model and the Reynolds-Stress model, were able to predict the mean turbulent velocity profile. However, in the region where turbulent shear becomes important (the logarithmic region), the Reynolds-Stress model outperformed the isotropic two-layer model (see Figure 5.2).

In the region very close to the wall where viscous shear is dominant, the mean velocity profile follows a linear viscous relation. This region is the *viscous sublayer* ($0 \leq y^+ \leq 5$). In the region where both viscous and turbulent shear are important, the velocity profile follows a logarithmic relation. As can be seen from Figure 5.2 the flow solver was perfectly able to resolve the viscous sublayer and the buffer layer. Commercial codes are not able to resolve these regions because of the small spacing requirements and the poor stability of their numerical schemes. Instead, commercial codes ignore the viscous sublayer and the buffer layer and compute the logarithmic region using the so called *logarithmic law of the wall*:

$$u^+ = \frac{1}{\kappa} \ln(y^+) + C \quad (5.4)$$

where κ and C are empirically determined constants. This approximation collapses for adverse pressure gradients and flow separation because of the assumptions made during its derivation. It will be made evident in the chapters to come, that the overall performance of the flow solver depends heavily upon the ability to resolve the viscous sublayer and buffer layer.

Also of interest and importance to the present study are the turbulence intensities in the three coordinate directions. Figure 5.3 shows a plot of the root-mean-square (r.m.s.) values of the fluctuating velocities computed by the Reynolds-Stress model.

Figure 5.3 also shows the associated isotropic fluctuations in the two-layer model ($2/3k$). We note that velocity fluctuations are higher in the dominant flow direction (the axial direction). Fluctuations in the radial and circumferential directions are small because the mean velocity in these directions is low. The anisotropy of the turbulence is clearly seen by comparing the predicted isotropic intensity ($2/3k$) to the predicted fluctuations in the three coordinate directions.

From the LDA and PIV measurements only the streamwise velocity fluctuations are obtained, and are compared to the computed values in Figure 5.4. The available experimental data is in excellent agreement with the computations. Despite the fact that PIV is better suited to study instantaneous flow structures rather than to generate flow statistics, the PIV measurements agree well with the numerical results. Close to the wall ($r/D \geq 0.4$) the PIV data is obscured by noise at small scales and hence larger r.m.s. velocities are obtained.

Figure 5.5 shows the Reynolds shear stress normalized by the shear stress at the wall. Shear stress near the wall is mostly due to its viscous component, hence the small values of Reynolds stress near the wall. Away from the wall, in the fully turbulent region, the Reynolds stress is the dominant component. The experimental data agrees well with the predictions.

The mean velocity profile normalized by the average velocity is shown in Figure 5.6. The Reynolds-Stress model and experimental results coincide for all r/D . Note that in the central region, where turbulent shear is dominant, the velocity profile is “flat” and is well correlated by a logarithmic profile (recall the law of the wall); as opposed to the parabolic profile for fully developed laminar flow.

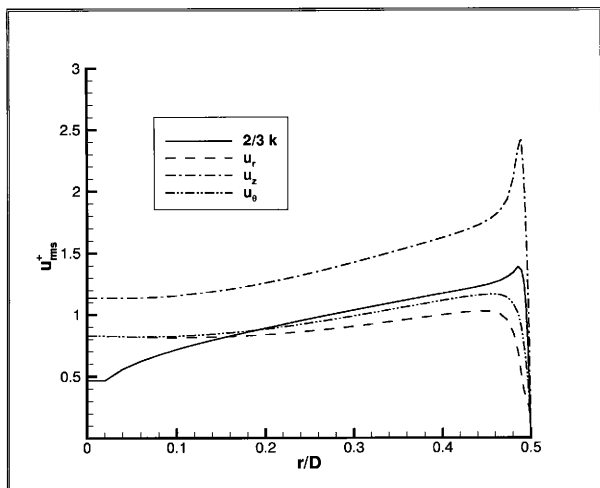


Figure 5.3: r.m.s. of the velocity fluctuations normalized by frictional velocity as a function of the distance from the centerline ($Re_D = 23000$)

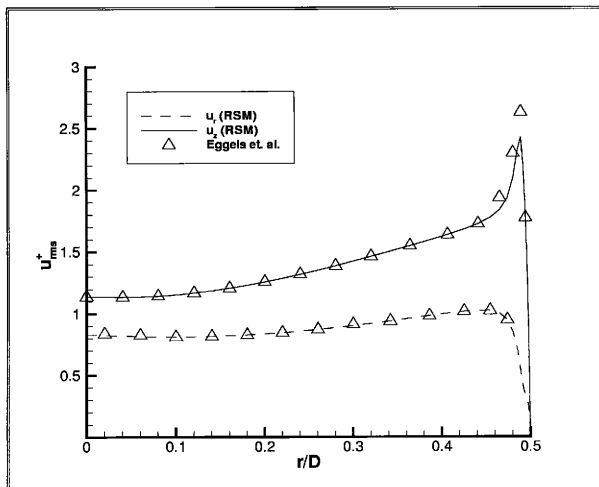


Figure 5.4: Numerical and experimental data for the streamwise fluctuating velocities ($Re_D = 23000$)

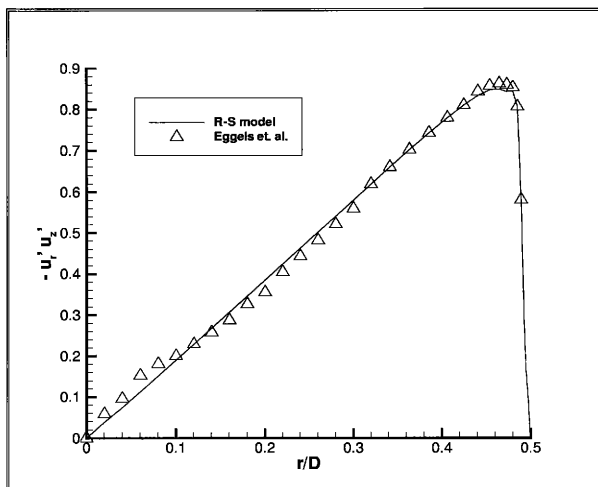


Figure 5.5: Reynolds shear stress normalized by the shear stress at the wall as a function of the distance from the centerline ($Re_D = 23000$)

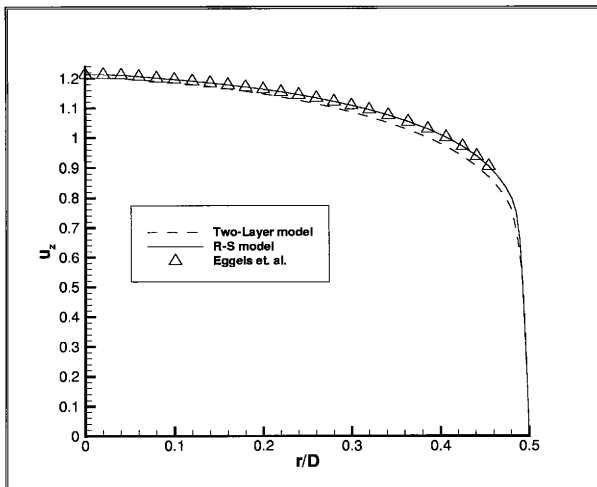


Figure 5.6: Axial mean velocity normalized by mean velocity ($Re_D = 23000$)

Chapter 6

Axisymmetric jet impinging on a flat plate

6.1 Geometry and Grid Generation

The grid generation was greatly simplified by the axisymmetric nature of the flow. The geometry and computational domain are shown schematically in Figure 6.1. Only three computational planes were required in the circumferential direction, two of which were used to impose the boundary conditions; making the problem two-dimensional, since only one plane was computed.

Simulations were performed for a fixed Reynolds number of $Re_D = 23,000$ at aspect ratios of $H/D = 2$ and 6. Profiles at the inlet were created by solving a fully developed turbulent pipe flow. The flow domain began at two pipe diameters upstream of the jet exit as shown in Figure 6.1, so that the fully developed turbulent profiles may evolve in the nozzle as the flow approaches the jet exit. The effect of the jet wall thickness on the flow was also properly modeled; the pipe wall thickness used

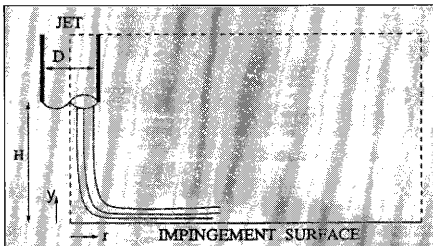


Figure 6.1: Geometry and computational domain

was equal to $0.0313D$. The effect of the right boundary location was examined and was found that once this was larger than $(8 + H/D)$, there was no noticeable effect on the flow field.

A fine, non-uniform, orthogonal, cylindrical grid of 35,000 grid points was used; with high resolution on all solid boundaries, including the thickness and outer boundaries of the pipe wall. The minimum grid spacing in the near-wall region was maintained at 10^{-4} of the body length which corresponds to a wall coordinate y^+ of the order of 0.1. An O-type grid was used around the pipe wall; the grid was first created by using Transfinite Interpolation (TFI) and then smoothed by solving the Laplace equation over the domain. This was deemed necessary in order to capture the details of the entrainment at the pipe exit. The O-type grid around the pipe wall is shown in Figure 6.2.

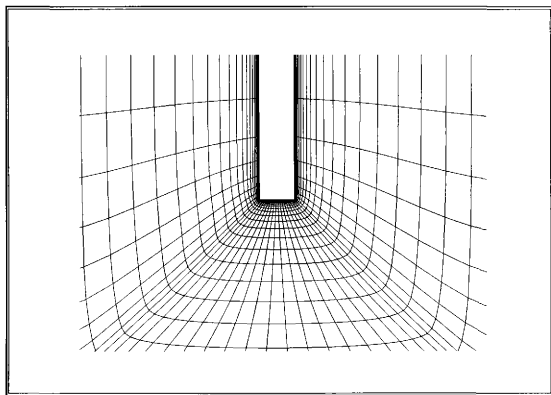


Figure 6.2: O-type grid around the pipe wall

6.2 Results and Discussion

6.2.1 Aerodynamics of impinging jets

The flow structure of impinging axisymmetric jets have been characterized and can be subdivided into three characteristic regions: the free jet region, the impingement (stagnation) flow region, and the wall jet region. In the free jet region, the shear-driven interaction of the exiting jet and the ambient produces entrainment of mass, momentum, and energy. The net effect includes development of a nonuniform radial velocity profile within the jet, expansion of the jet, an increase in total mass flow rate, and modification of the jet temperature before it impinges on the surface. Figure 6.3 shows the computed mass and momentum entrainment represented by the velocity vector field.

The impingement zone is characterized by a stagnation region and the turning of the jet in the radial direction, which affects a transition for a wall jet further downstream. High pressure and low velocities are expected at the stagnation region. Figure 6.4 shows the predicted normalized pressure contours at the stagnation region for $H/D = 2$. Note that there is a small pressure gradient at the exit of the jet, no pressure gradient in the free jet region, and high pressure gradients near the stagnation region. The high pressure gradients here are caused by the sudden turning of the jet, i.e. the rapid decrease of the axial velocity component.

Within the stagnation region, flow is decelerated and accelerated in the axial and radial directions respectively. As the jet leaves the stagnation region there is a bulk flow outward in the radial direction. However, since the flow continues to entrain zero momentum fluid from the ambient, radial acceleration cannot continue indefinitely and accelerating flow in the stagnation region is transformed to a decelerating wall jet.

Hence, with increasing r , velocity components parallel to the surface increase from a value of zero to some maximum and subsequently decay to zero. Velocity profiles within the wall jet are characterized by zero velocity at both the impingement and free surfaces. Figure 6.5 shows the velocity magnitude contours for $H/D = 2$ at the stagnation region and the wall jet region. Note that the radial velocity maximum occurs at approximately one jet diameter from the impingement zone. The contours also show the potential core of the jet; defined as the region of the jet where the axial velocity remains constant and equal to the nozzle exit velocity. Here, the potential core cannot extend to its full length because of the small nozzle-plate spacing. Figure 6.5 also shows the decay of the axial velocity profile caused by the large shear stresses at the jet boundary.

The impinging potential core of the free jet contains low levels of turbulence and these should remain relatively low in the stagnation region. The two-layer model and Reynolds-Stress model predictions are consistent with this expectation. Turbulent kinetic energy contours predicted for $H/D = 6$ with the isotropic two-layer model are shown in Figure 6.6. The maximum value of k predicted by the two-layer model occurs away from the stagnation region at $r/D \approx 1$.

Turbulent kinetic energy contours predicted with the Reynolds-Stress model are shown in Figure 6.7. Again, the maximum value of k occurs away from the stagnation region at $r/D \approx 1$. The maximum values of k predicted by both models differ by 8%. The isotropic two-layer model was able to predict a very accurate turbulent kinetic energy. However, this does not imply that the turbulence intensities associated with a jet impinging on a flat plate are nearly isotropic. The high performance of the isotropic model in predicting the turbulent kinetic energy field is attributed to the two-layer approach used in the turbulence modeling and to the capacity of the flow solver to resolve the viscous sublayer and buffer layer.

The normalized velocity fluctuations in the radial direction are shown in Figure 6.8. The radial velocity fluctuations in the free jet are small because radial mean velocity in this region is not significant and turbulence intensities at the exit of the pipe are quite low. As the jet approaches the wall jet region and leaves the stagnation region, $\overline{u_r^2}$ becomes a maximum. This increase arises from the acceleration of the mean radial velocity and the deceleration of the mean axial velocity. The turbulence intensity diminishes deep into the wall jet region because of the entrainment of low turbulence fluid and the decelerating radial velocity. The increase at greater distance from the wall simply reflects a more energetic part of the turbulent mixing layer.

Figure 6.9 shows the normalized velocity fluctuations contours in the axial or normal to the plate direction. The axial velocity fluctuations in the free jet are as high as the radial velocity fluctuations at beginning of the wall jet region. The maximum value of $\overline{u_x^2}$ is the maximum value of all the velocity fluctuations and occurs away from the stagnation region. The high value arises from the pressure-strain process and from the axial mean velocity falling to zero, i.e. the shear induced by the flow acceleration away from the stagnation region. As the jet moves into the wall jet region, axial velocity fluctuations decrease rapidly due to the small axial mean velocity component in this region.

Normalized fluctuations in the circumferential direction are shown in Figure 6.10. Fluctuations in this direction are negligible relative to the other two components.

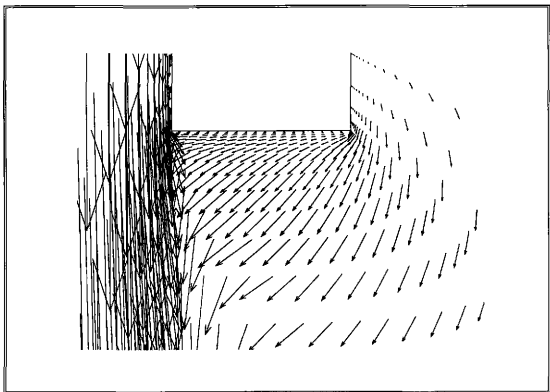


Figure 6.3: Mass and momentum entrainment shown by velocity vectors

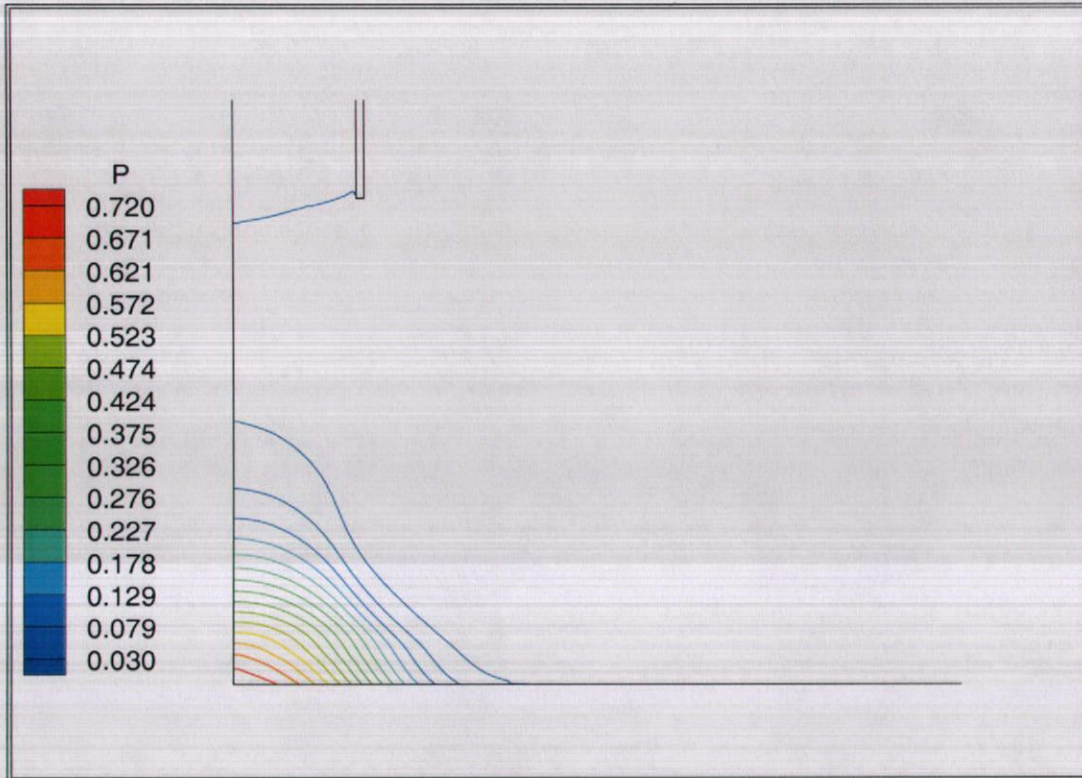


Figure 6.4: Normalized pressure contours at the stagnation region for $H/D = 2$ and $Re_D = 23,000$

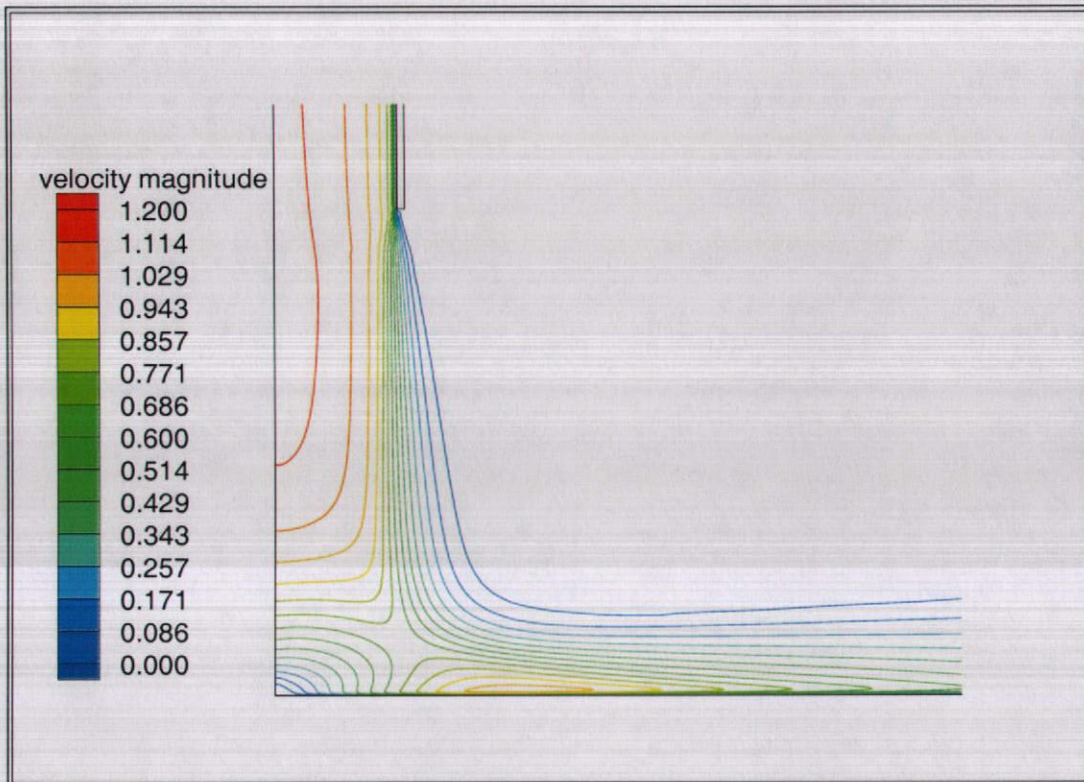


Figure 6.5: Normalized velocity magnitude contours at the stagnation region and wall jet region for $H/D = 2$ and $Re_D = 23,000$

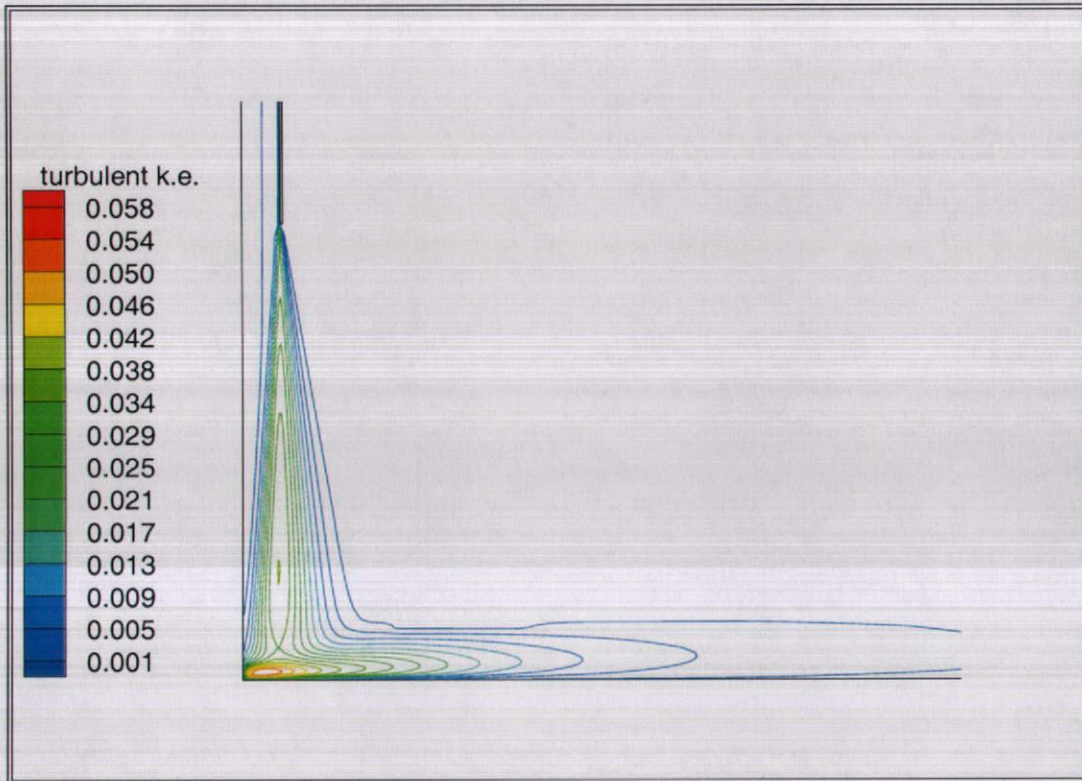


Figure 6.6: Normalized turbulent kinetic energy contours by two-layer model for $H/D = 6$ and $Re_D = 23,000$

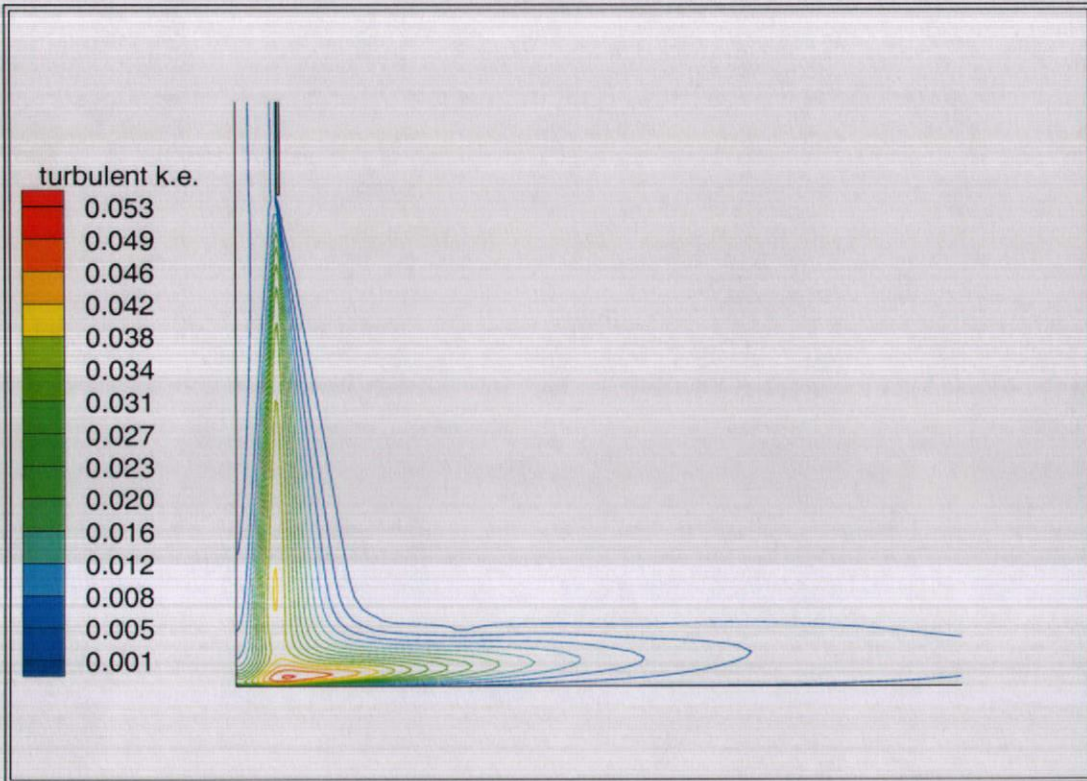


Figure 6.7: Normalized turbulent kinetic energy contours by Reynolds-Stress model for $H/D = 6$ and $Re_D = 23,000$

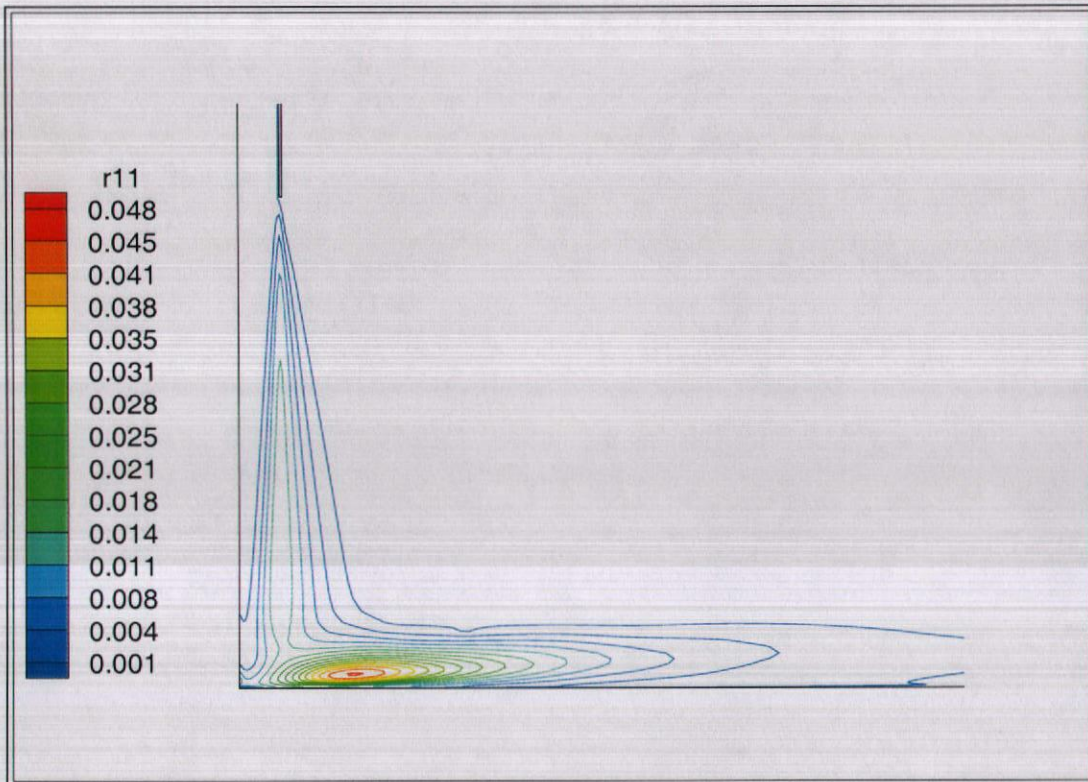


Figure 6.8: Radial velocity fluctuations squared $\left(\overline{u_r^2}\right)$ by Reynolds-Stress model for $H/D = 6$ and $Re_D = 23,000$

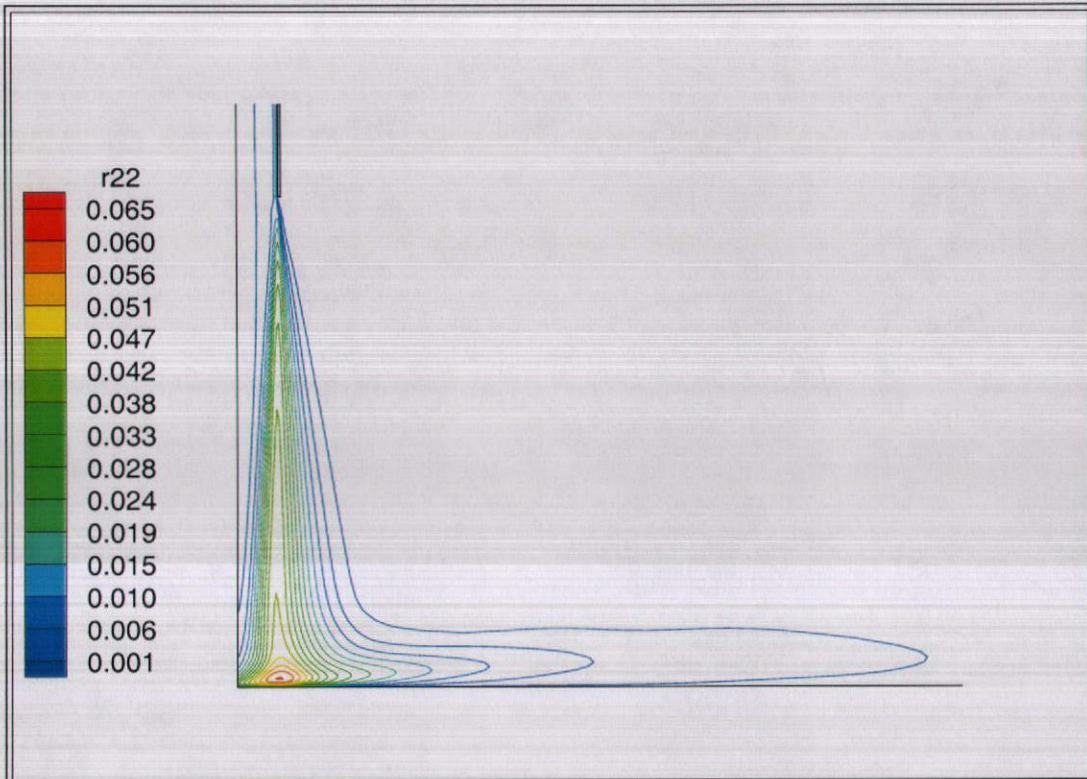


Figure 6.9: Axial velocity fluctuations squared $\left(\overline{u_y^2}\right)$ by Reynolds-Stress model for $H/D = 6$ and $Re_D = 23,000$

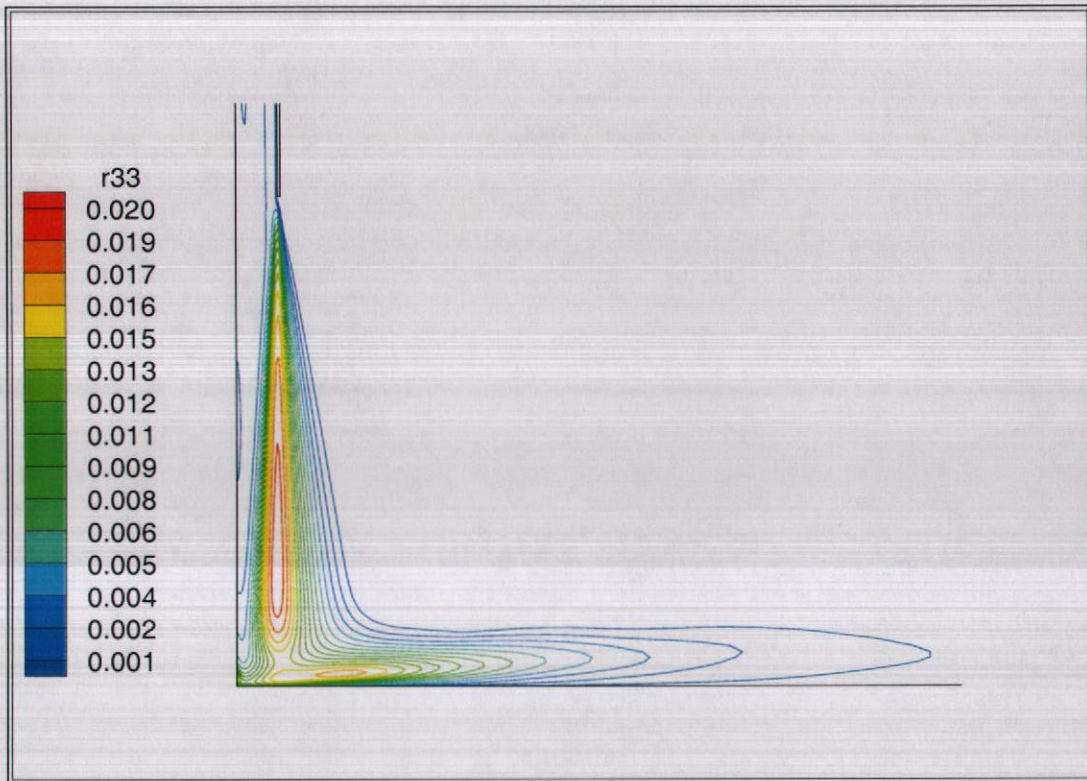


Figure 6.10: Circumferential velocity fluctuations squared ($\overline{u_\theta^2}$) by Reynolds-Stress model for $H/D = 6$ and $Re_D = 23,000$

6.2.2 Heat Transfer

As the cold jet impinges on the heated surface, heat transfer by convection takes place between the moving fluid and the heated surface. To quantify the heat transfer near the surface of the heated plate we compute the Nusselt number, defined as:

$$Nu_D = \frac{hD}{K} \quad (6.1)$$

where K is the thermal conductivity of the fluid, D is the diameter of the pipe, and h is the local convective heat transfer coefficient defined by:

$$h = \frac{q}{(T_{wall} - T_{jet})} \quad (6.2)$$

where q is the convective heat flux. We can rewrite equation 6.2 by using Fourier's law and express the convective heat flux in terms of the temperature gradient at the wall:

$$h = \frac{-K}{(T_{wall} - T_{jet})} \left(\frac{\partial T}{\partial y} \right)_{y=0} \quad (6.3)$$

Combining equations 6.1 and 6.3, we may write the Nusselt number in terms of the normalized temperature gradient at the wall:

$$Nu_D = \left(\frac{\partial T^*}{\partial y^*} \right)_{y^*=0} \quad (6.4)$$

Figure 6.11 shows the the predicted local Nusselt number distribution along the radial direction, with $r/D = 0$ being the stagnation point. The results shown were

computed with the isotropic two-layer $k - \epsilon$ model and are compared with the experimental data of Lytle and Webb [12] and the predictions of Durbin's isotropic $k - \epsilon$ model [13].

Durbins's standard $k-\epsilon$ model overpredicted the stagnation Nusselt number by as much as 100%. while our two-layer $k-\epsilon$ model underpredicted by as much as 7%. The only difference between the two isotropic models is that the two-layer $k-\epsilon$ model of Chen and Patel [3] is able to resolve the viscous sublayer and buffer layer, whereas Durbin's standard $k-\epsilon$ uses the law of the wall to resolve the inner layer. This indicates that the resolution of the viscous sublayer and the buffer zone is of critical importance in heat transfer predictions.

This is readily understood by realizing that in the two-layer model the velocity gradient at the wall is computed directly, rather than being extrapolated from the logarithmic region, as is the case in the standard $k-\epsilon$. Furthermore, the velocity gradient at the wall is used to compute the temperature profile and consequently the local heat transfer coefficients.

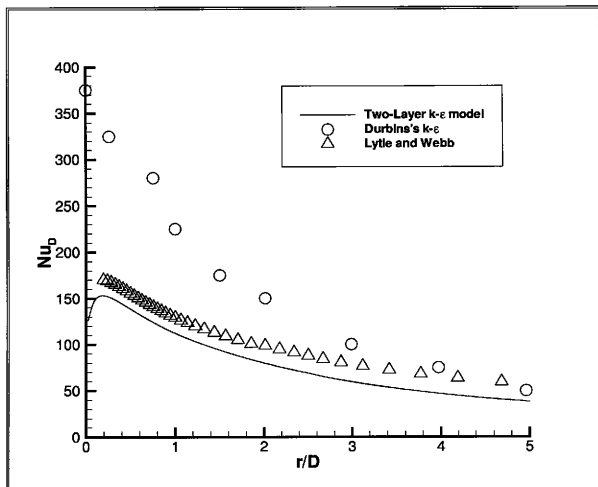


Figure 6.11: Nusselt number distribution for $H/D = 6$ and $Re_D = 23,000$

Chapter 7

Impinging jet on the leading edge of a turbine blade

7.1 Geometry and Grid Generation

The geometry for the leading edge of the turbine blade was taken from the experimental test section of Bunker and Metzger [14]. The test section is composed of a plenum chamber and the airfoil. The plenum chamber has a diameter R of 7.62 cm, a wall thickness of 0.95 cm, and a height of 40.64 cm. The impinging jets issue through nozzles of diameter D , which are placed symmetrically along the plenum apex at a uniform spacing (pitch) C between jet centerlines. The present computation utilized a plenum with pitch-to-jet diameter ratio of $C/D = 4.67$. The airfoil had a radius of curvature $r^* = R/D$ equal to 0.4. The jet-nozzle to apex spacing was kept at $z/D = 3.04$. The symmetric behavior of the flow and the shape of the test section allowed for the modeling of only on quarter of a pitch. Figure 7.1 shows a two-dimensional top view of the model.

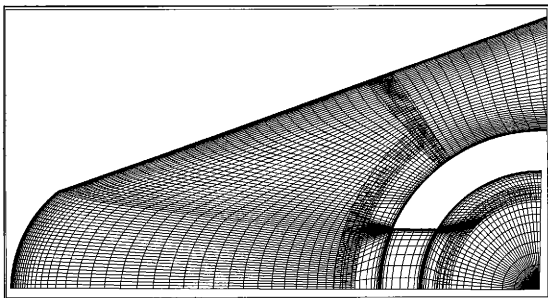


Figure 7.1: Top view of the computational domain

Cold, uniform flow with $U^* = 0.085$ enters the plenum at $t = 0$. The magnitude of the uniform velocity profile at the inlet was chosen such that $U_{jet}^* = 1.0$ at the inlet of the jet-hole. As can be seen from Figure 7.1, the velocity of the fluid will increase because of the reduction in area of the plenum. The cold jet issues through the nozzle, impinges on the heated leading edge of the airfoil, and exits the test section through an expanding duct. The Reynolds number based on the jet diameter D and mean velocity was equal to $Re_D = 25,000$.

The numerical grid was generated using *GRIDGEN*. It was then reblocked into several interlocked computational blocks to facilitate the implementation of near-wall turbulence models and specification of boundary conditions. To provide adequate resolution of the viscous sublayer and buffer layer adjacent to a solid surface, the minimum grid spacing in the near-wall region is maintained at 10^{-4} of the body length which corresponds to a wall coordinate y^+ of the order of 0.1. This can be

seen from Figure 7.1, by the dense grid point regions in the “wal” surfaces. Also note the overlap between adjacent blocks, needed in order to implement the composite overset multi-block method.

Figure 7.2 shows a full three-dimensional view of the multiblock volume grid used to obtain the final flow and temperature fields. A total of three preliminary volume grids were constructed before the one shown on Figure 7.2. This volume grid has a total of 400,000 grid points and uses eight blocks; some of them fully connected and some overset. Different blocks are shown in different colors.

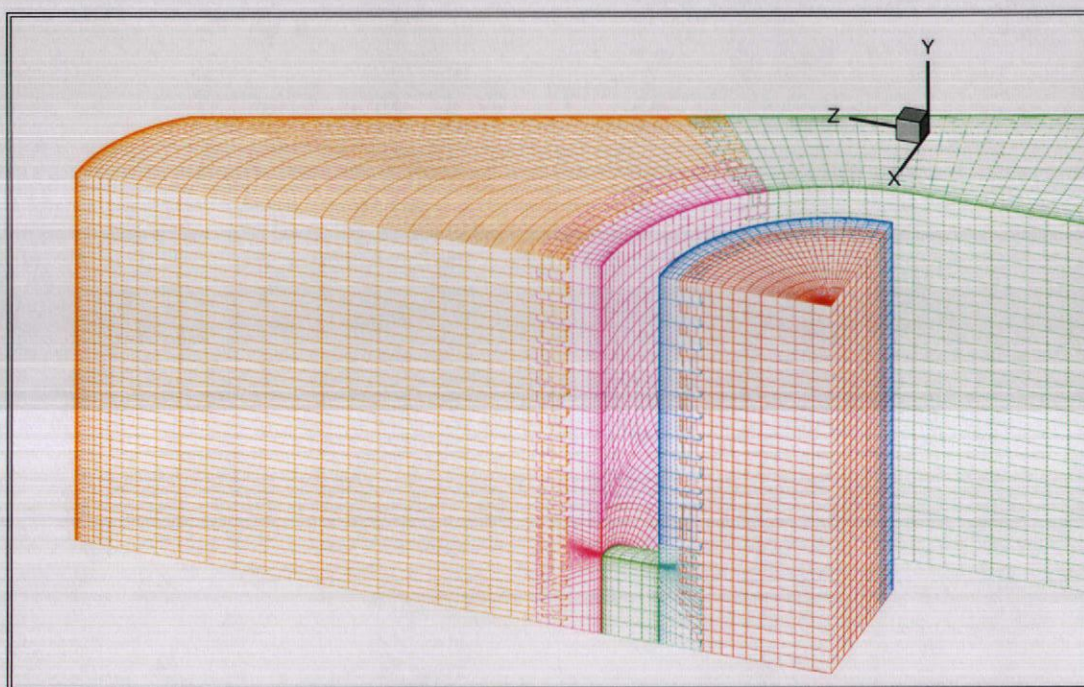


Figure 7.2: Three-dimensional geometry and coordinate system

The first numerical grids generated were coarse (around 100,000 grid points) and made extensive use of the *Chimera* method to obtain adequate resolution in geometrically difficult areas. Of particular interest is the plenum-hole-airfoil intersection,

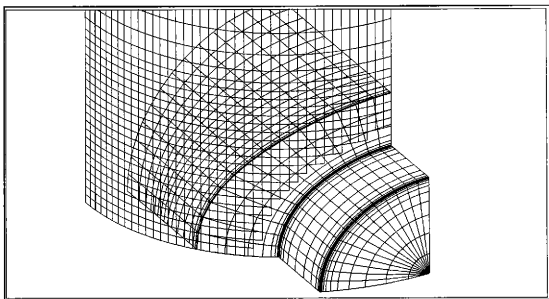


Figure 7.3: Plenum-hole-airfoil Chimera intersection

shown in Figure 7.3.

The first attempt was to have the cylindrical grid defining the hole, cut through part of the plenum and the airfoil, as shown on Figure 7.3. However, it was found that the point donation between adjacent blocks in the near-wall region was of unacceptable quality due to the small spacing in this region. This led to poor communication between blocks, which showed as discontinuities in the numerical solution of the flow and temperature fields. The problem was solved by making the plenum-hole-airfoil intersection fully connected in subsequent grids, as shown in Figure 7.4. The *Chimera* method, continued to be implemented, but this time away from the near-wall region.

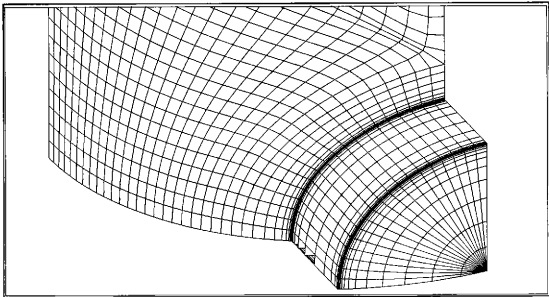


Figure 7.4: Plenum-hole-airfoil fully connected intersection

7.2 Results and Discussion

7.2.1 Turbulent flow field analysis

The present computation differs from that presented in Chapter 6 in the following aspects:

- Now, the jet is confined,
- the impingement surface is no longer flat but highly concave,
- and finally, the jet belongs to an array of jets.

Although only one jet was needed for the simulation, the rest of the jets were accounted for via Neumann boundary conditions at the symmetry planes. The computation was performed with the isotropic two-layer model only, the Reynolds-Stress model was not implemented due to time constraints.

Uniform flow enters the plenum and is accelerated towards the inlet of the nozzle by the plenum's reduction in cross-sectional area. Just after the nozzle, the flow has the distinctive characteristics of a jet. It expands with an angle of about 10° and entrains the surrounding fluid. Figure 7.5 shows the velocity magnitude contours on the spanwise symmetry plane. Over a distance of about $1.5D$ the velocity remains constant as in the potential core of a free jet. Then the velocity decreases strongly under the influences of both turbulent diffusion and flow confinement. Turbulent diffusion is responsible for the transfer of momentum from the axis to the surrounding fluid similar to a free turbulent jet. However, in contrast to the unbounded case in which the total flux of momentum remains nearly constant with the distance, for the present geometry, the total mass flux must remain constant with z . The mixing

process causes the velocity profile to flatten with z and the total momentum flux to decrease. This decay can only be compensated by an adverse pressure gradient (Figure 7.6) which, in turn, makes the velocity drop faster with z .

As the jet impinges on the leading edge, it attaches to the leading edge surface and moves in the chordwise direction. The adverse pressure gradient caused by the decay of the momentum flux (shown in Figure 7.6) causes the attached fluid to separate and form the recirculation region shown in Figure 7.7.

In the potential core, the velocity gradients are negligible and the turbulence level is weak. Turbulence levels are shown in Figure 7.8 as turbulent kinetic energy contours. The fluctuations are induced by the growing mixing layer and increase from the jet exit. Farther away than $z \approx D$, owing to high strain rate turbulence, production leads to intense turbulence at the jet boundary. As in unbounded jets, the turbulent kinetic energy decreases with z due to the diminution of the velocity gradient. Before impingement, the turbulence energy is redistributed from the axial component to the other components.

Near the stagnation region, at the location where the cross-section area of the jet occupies more than half of the leading edge region ($z = 2.5D$), the effect of the chordwise or lateral confinement becomes significant. There exists a core of near constant radius in which the velocity is positive. This core is surrounded by an annular layer in which the velocity is negative (Figures 7.9 and 7.10). At the core boundary, the radial component of the mean velocity is directed towards the wall. Hence, the bulk velocity decreases with z . Owing to the lateral confinement, the mean flow structure has drastically changed with respect to the region of expansion. Nevertheless, the turbulence is still dominated by similar mechanisms involving production, advection, and dissipation.

The kinematic structure of mean and turbulent properties of the velocity field on the jet axis show some peculiarities of the flow behaviour. Indeed, both lateral (chordwise) confinement due to the blade wall (Figure 7.5) and longitudinal (spanwise) confinement caused by the leading edge of the blade (Figure 7.11), compel the flow to restructure from a typical shear flow to a decaying diffusive turbulence. The transition between these two states involves different successive steps. The first step takes place in the region dominated by the mean velocity. The interaction of the mean flow with the blade wall causes the jet expansion to stop. The second step is more gradual and has been described by Fitzgerald and Garimella [15]. The mean velocity decreases and the flow becomes dominated by the turbulence near $z = 2.5D$. As the turbulence level is not maintained by production, it decays with z and the size of the larger eddies increases. The third step is when their size reaches the tube diameter. They stop growing and the turbulent scale is controlled by the tube diameter.

Contrary to our expectations, the predicted turbulent flow field shows that once the flow leaves the stagnation region, the bulk of the flow moves in the spanwise direction instead of the chordwise direction; as shown by Figures 7.5 and 7.11.

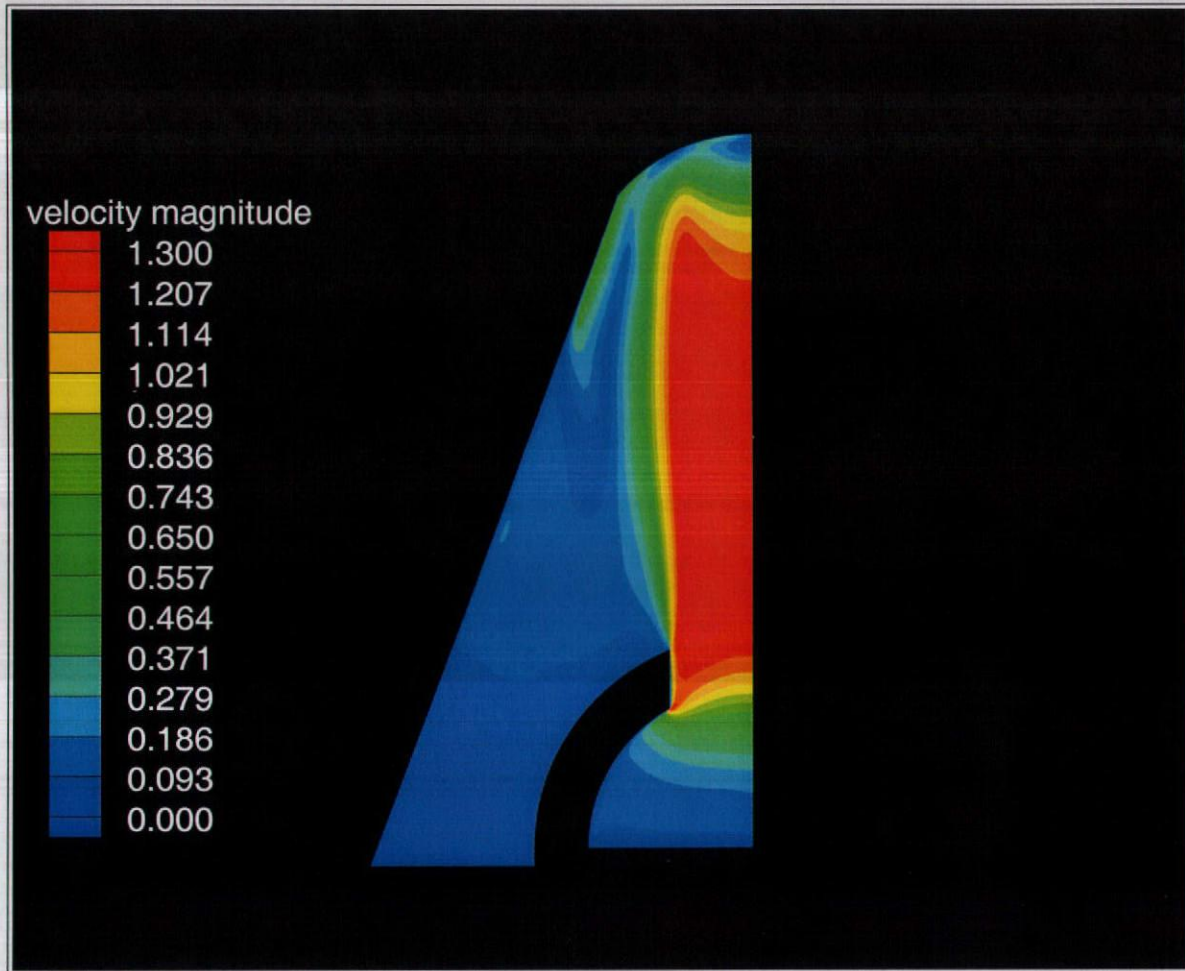


Figure 7.5: Normalized velocity magnitude contours on the spanwise symmetry plane for $Re_D = 25,000$

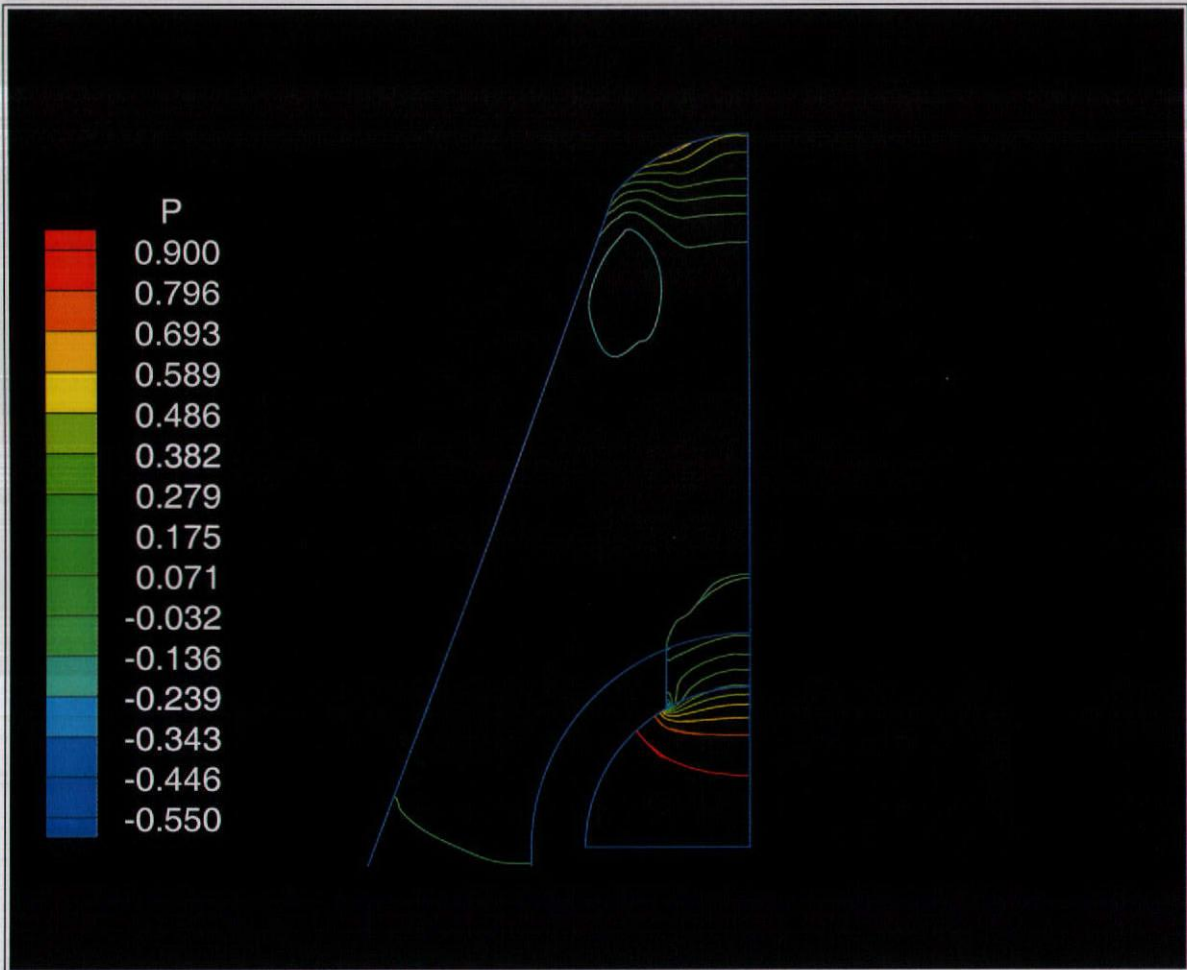


Figure 7.6: Normalized pressure contours on the spanwise symmetry plane for $Re_D = 25,000$

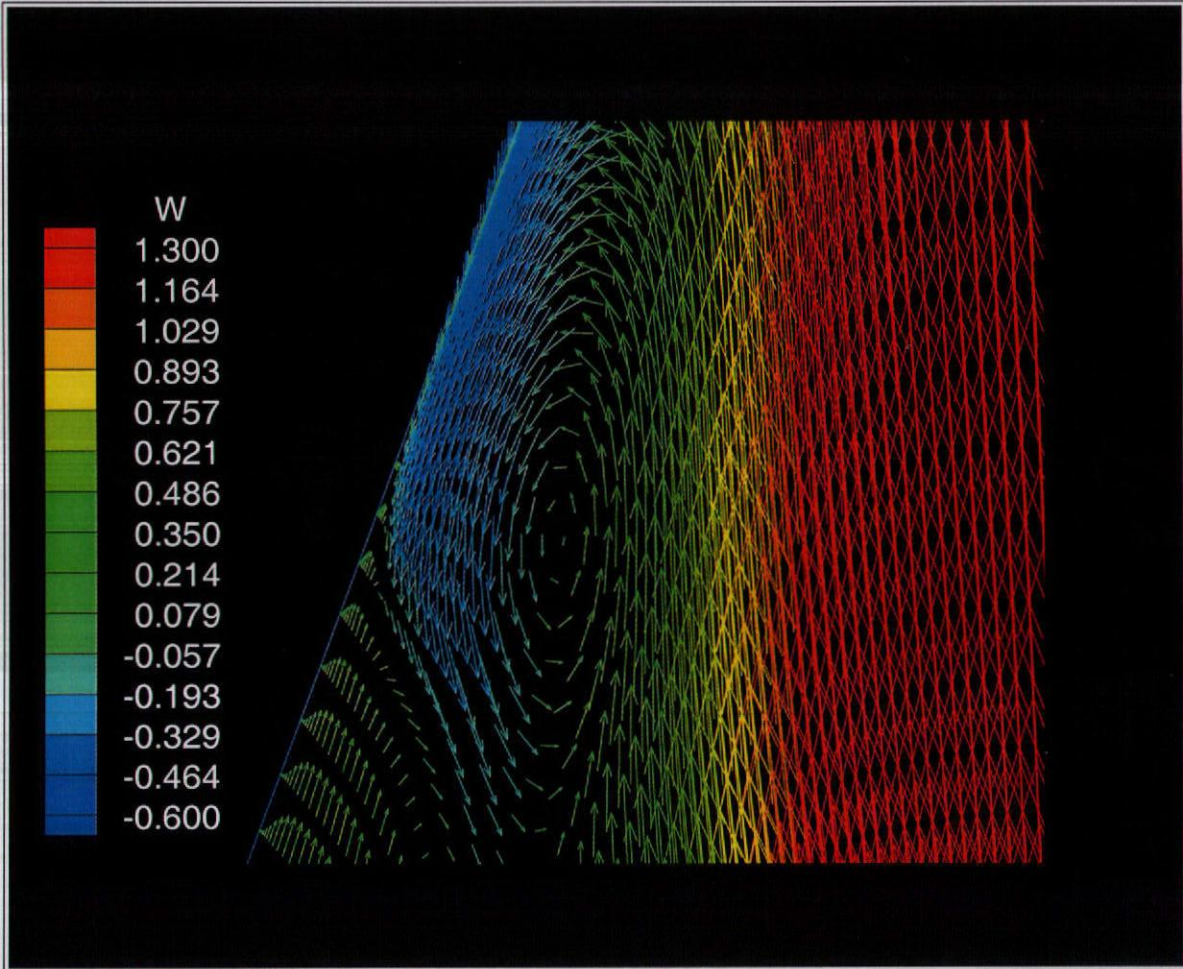


Figure 7.7: Velocity vector field showing the recirculation region on the spanwise symmetry plane for $Re_D = 25,000$

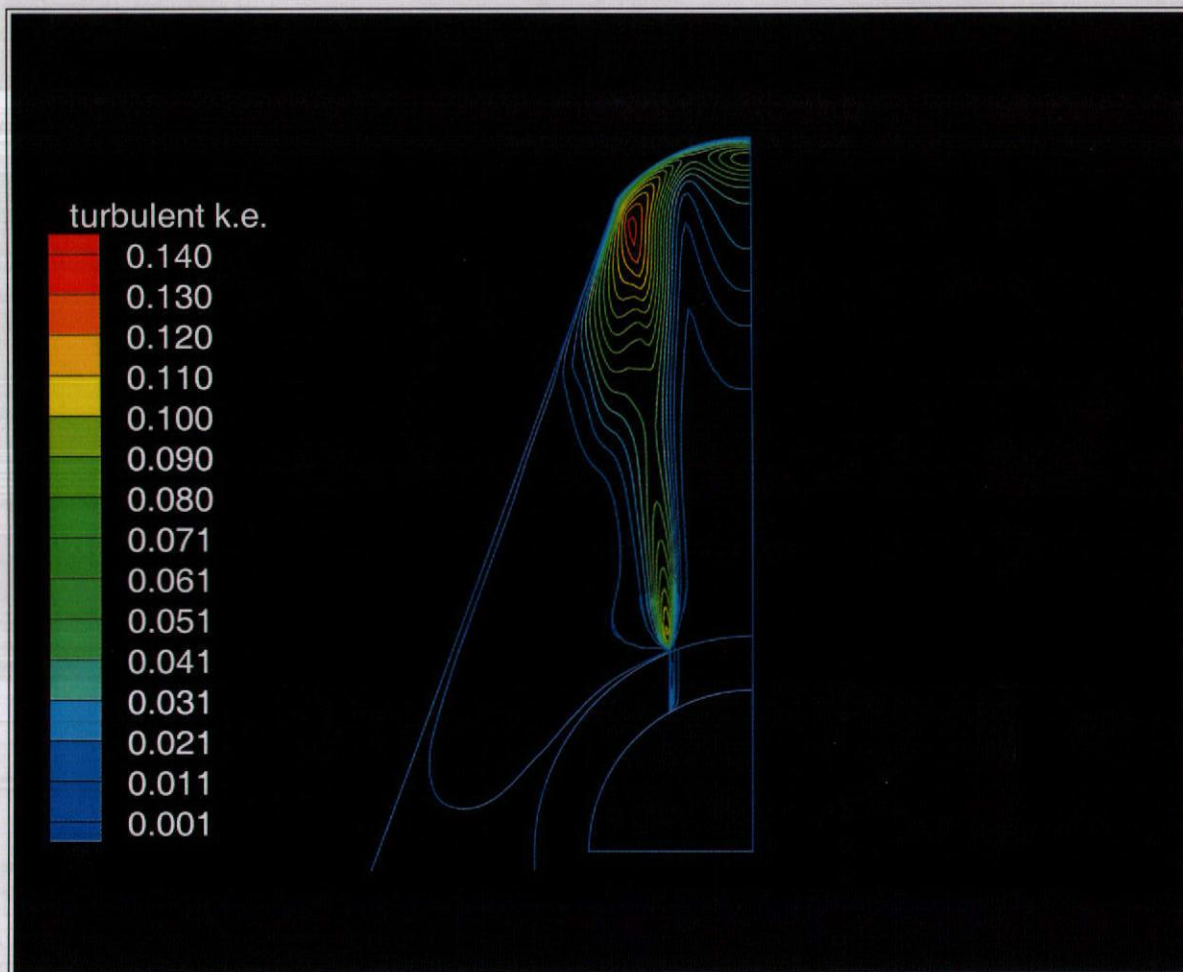


Figure 7.8: Turbulent kinetic energy contours on the spanwise symmetry plane for $Re_D = 25,000$

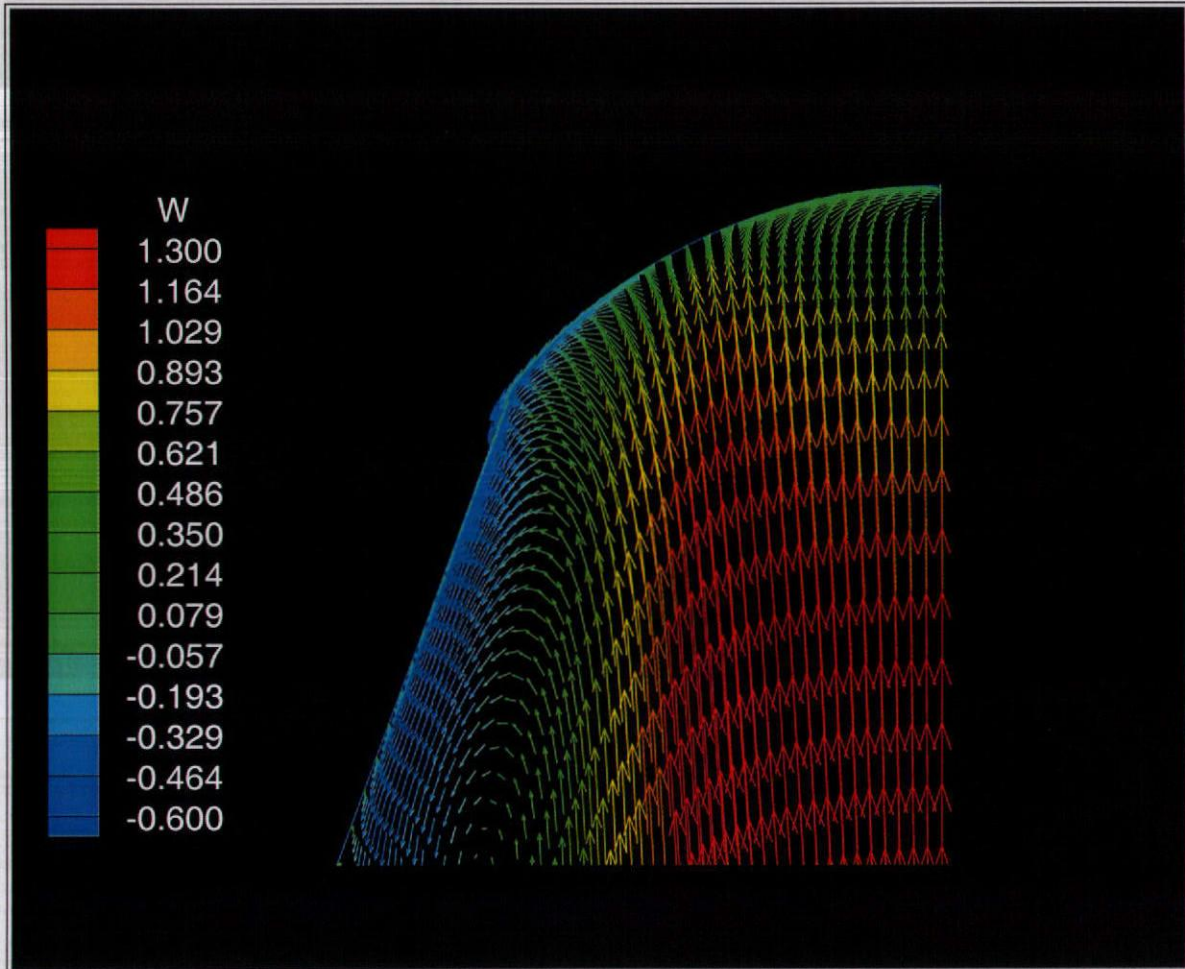


Figure 7.9: Velocity vector field in the spanwise symmetry plane colored by axial (z) velocity for $Re_D = 25,000$

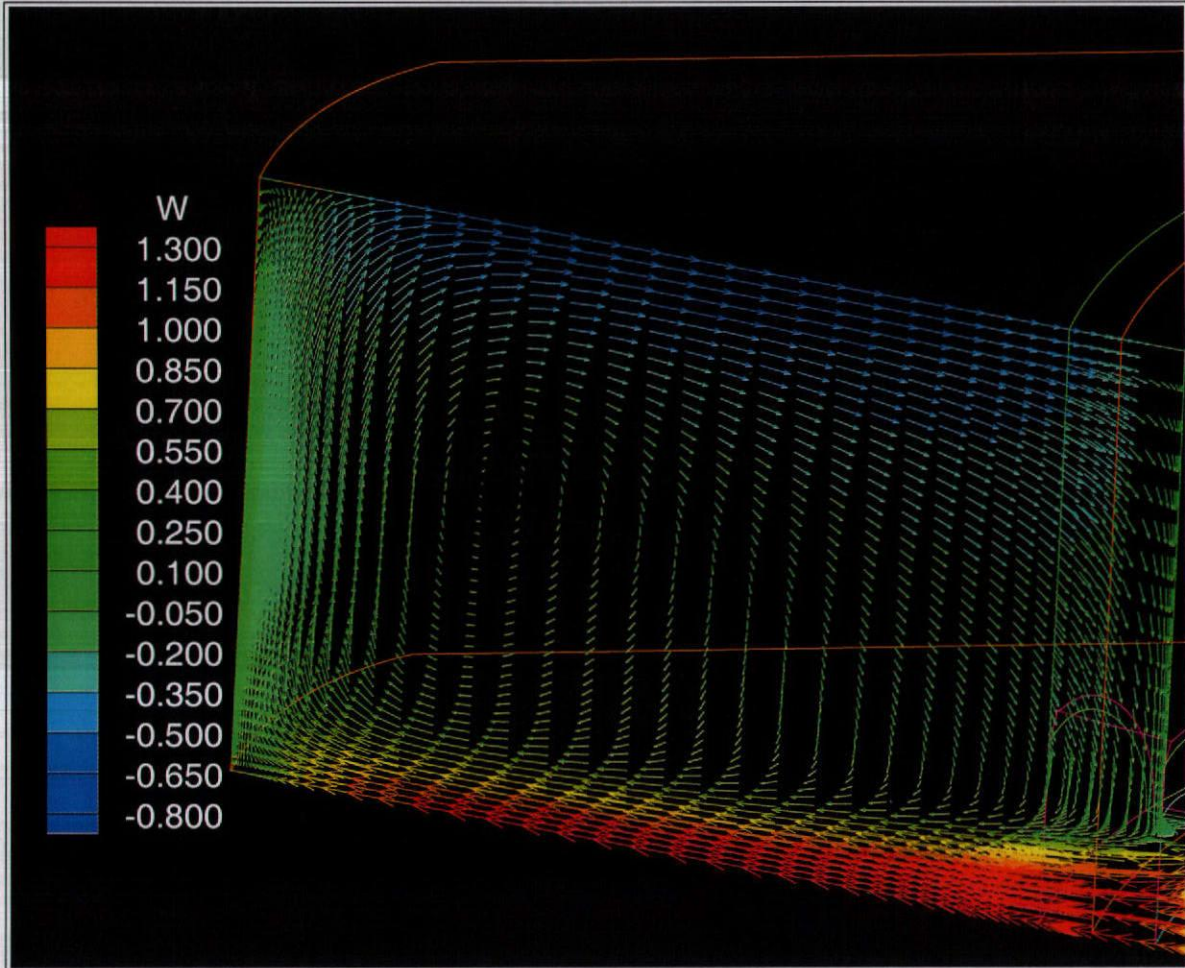


Figure 7.10: Normalized velocity vector field in the chordwise symmetry plane for $Re_D = 25,000$

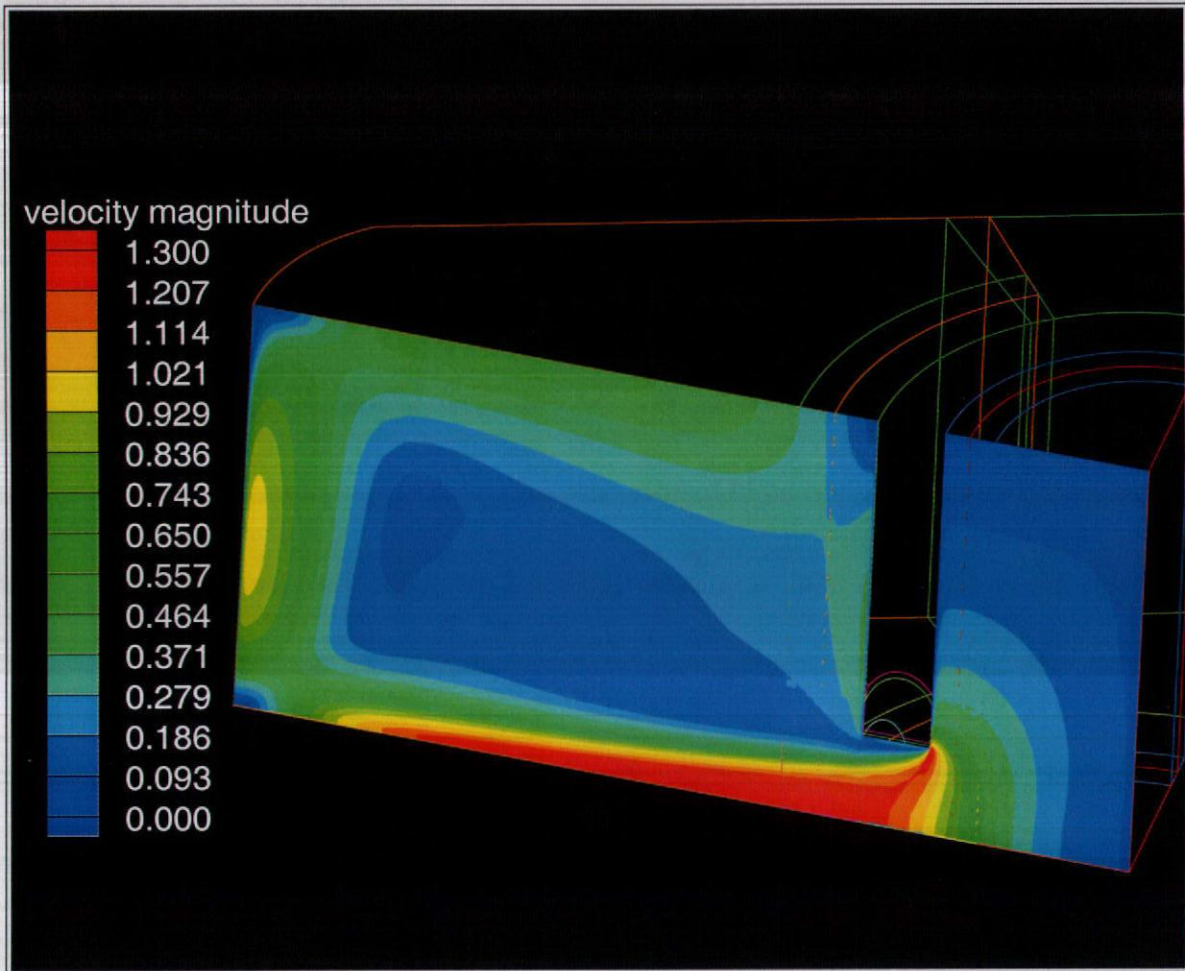


Figure 7.11: Normalized velocity magnitude contours on the chordwise symmetry plane for $Re_D = 25,000$

7.2.2 Heat Transfer

Figure 7.12 and 7.13 show the predicted temperature field in the spanwise and chordwise symmetry planes respectively. As the cold jet issues through the nozzle and starts to entrain fluid we see a small temperature gradient at the beginning of the shear flow region. As the jet approaches the leading edge endwall, the lateral confinement causes the jet to stop growing and to “spray” its cold potential core onto the heated leading edge endwall.

The local heat transfer distribution on the leading edge of the airfoil was computed in terms of Nusselt number and is shown in Figure 7.14. The maximum Nusselt number occurs near the stagnation region and decreases gradually in the spanwise direction. The abrupt change in Nusselt number in the chordwise direction is attributed to the bulk movement of the flow in the spanwise direction instead of the chordwise direction. We believe that this abrupt change is due to a geometry modeling problem brought about the poor description of the geometry of the test section in the Bunker and Metzger publication [14]. However, the Nusselt number distribution on the endwall of the leading edge region is physically correct and close to experimental data, especially in terms of spanwise average Nusselt number.

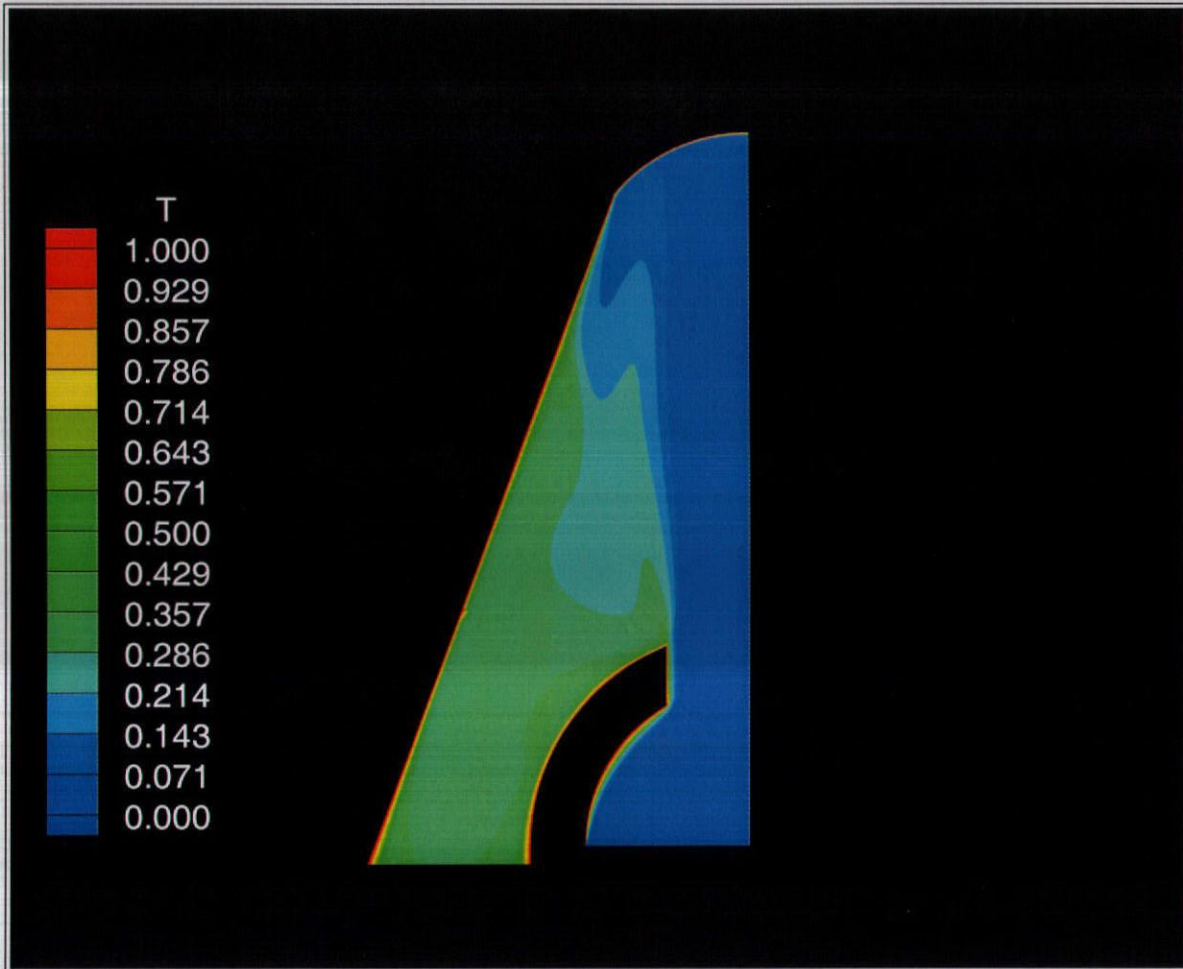


Figure 7.12: Normalized temperature contours on the spanwise symmetry plane for $Re_D = 25,000$

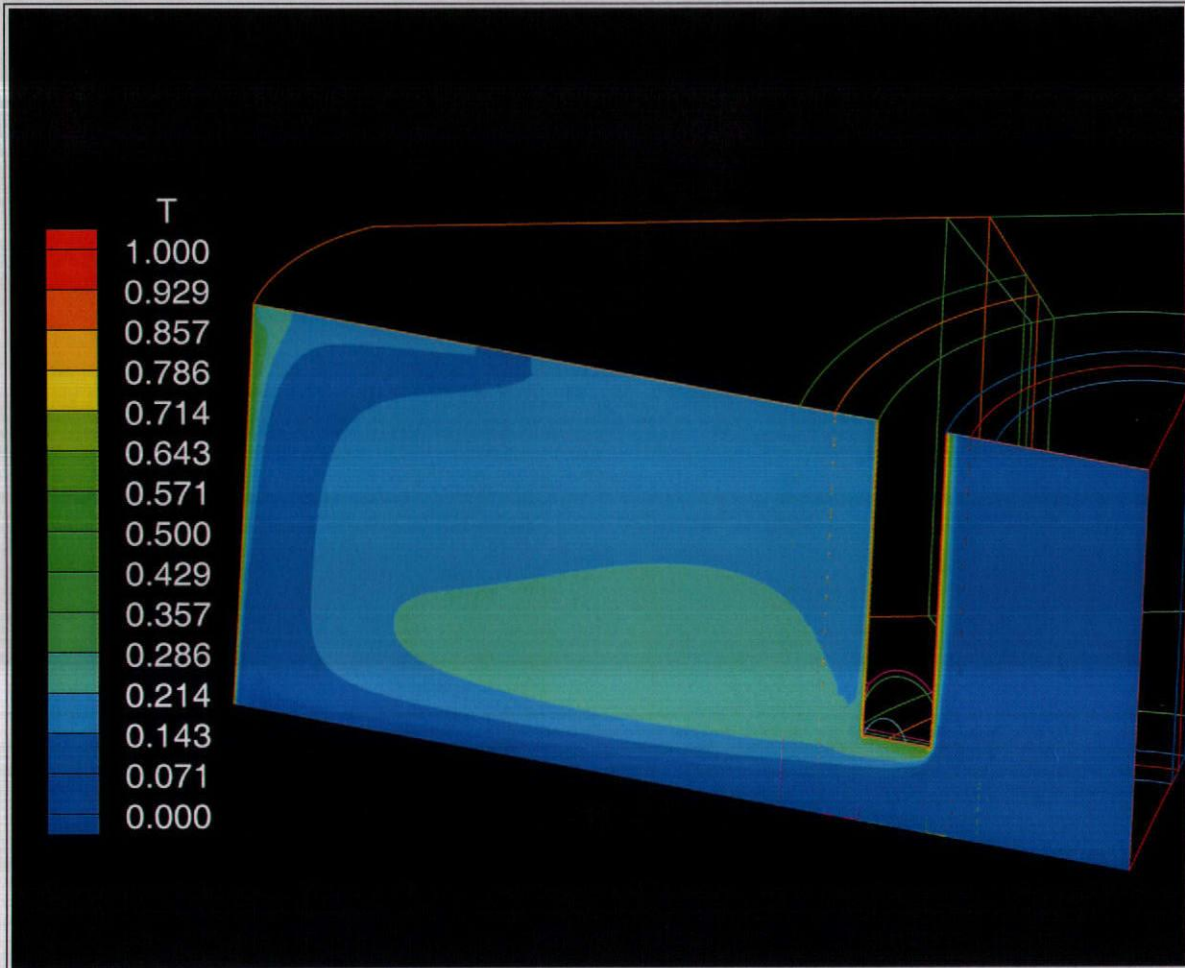


Figure 7.13: Normalized temperature contours on the chordwise symmetry plane for $Re_D = 25,000$

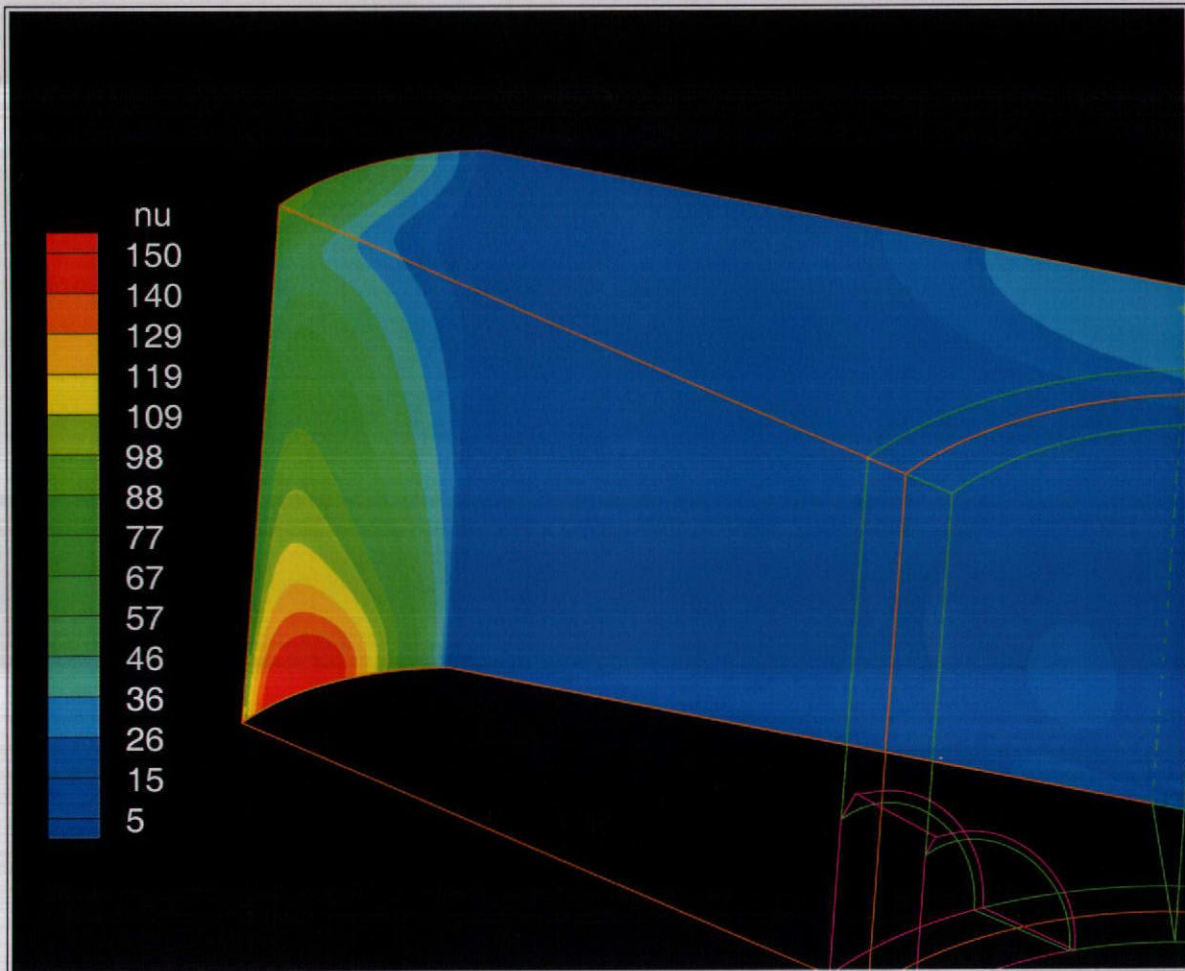


Figure 7.14: Local nusselt number distribution on the leading edge of the airfoil for $Re_D = 25,000$ and $z/D = 3.04$

Chapter 8

Conclusions and Recommendations

The present investigation was concerned with the implementation of a numerical method to solve the governing equations of fluid flow and heat transfer in order to predict the turbulent flow field and local heat transfer coefficients in the leading edge region of an impingement cooled gas turbine airfoil. The computations have covered an extensive programme to assess the turbulence models and to study the physics of impingement in a simple geometry, i.e. the axisymmetric jet impinging on a flat plate. This research has successfully achieved the objective of showing the anisotropy of turbulence in the impingement problem and providing information on the turbulent flow field and local heat transfer distribution on the leading edge region of the airfoil.

8.1 Conclusions

The specific conclusions of the study are:

- The Reynolds-Averaged Navier-Stokes equations were solved to examine the aerodynamics of an axisymmetric jet impinging on a flat plate. The anisotropy

of the turbulence quantities was shown and explained in terms of mean velocity gradients, entrainment of zero momentum fluid, and the pressure-strain process.

- The near wall resolution of the viscous sublayer and buffer layer is crucial when attempting to predict local heat transfer coefficients. This was demonstrated when the predicted local Nusselt number profile using the two-layer model was compared to experimental data and standard k - ϵ results.
- A turbulent flow field analysis of the impinging jet on the leading edge of the turbine was performed and showed that just after the nozzle, the flow has the characteristics of a jet: expansion and entrainment. The mean velocity of the flow decreased as it approached the leading edge due to flow confinement and turbulent diffusion. The recirculation region observed in the symmetry plane of the airfoil was explained in terms of an adverse pressure gradient resulting from the rapid decay of the mean velocity gradient and the momentum flux. Heat transfer on the endwall of the leading edge region was explained in terms of the kinematic structure of the flow field.

8.2 Recommendations

The following recommendations are made for a future study:

- Due to time constraints, the present study dealt with a fixed Reynolds number of $Re_D = 25,000$, a fixed pitch-to-jet diameter ratio of $C/D = 4.67$, a fixed radius of curvature equal to $r^* = 0.4$, and a fixed target spacing of $z/D = 3.04$. It would be desirable to design a computational programme to deal with at least four different Reynolds numbers, three different pitch-to-jet diameter ratios, two radii of curvature, and at least six different target spacings. This would

be done with the purpose of studying the effect of each parameter on the local heat transfer distribution on the leading edge of the airfoil. The results could also be used to form a database for the purpose of designing cooling schemes for turbine airfoils.

- This investigation dealt with impingement cooling on the leading edge of a blade without showerhead bleed. It would be desirable to include showerhead bleed on the leading edge to study its effect on the local heat transfer distribution. Showerhead bleed hole positioning could also be studied.
- The present study dealt with a non-rotating airfoil. The effects of rotation on the turbulent flow field and local heat transfer coefficients should be studied in future work.

References

- [1] Chen, C.J. and Chen, H.C., "Finite-Analytic Numerical Method for Unsteady Two-Dimensional Navier-Stokes Equations," *Journal of Computational Physics*, Vol. 53, 1984, pp. 209-226.
- [2] Patankar, S.V., *Numerical Heat Transfer and Fluid Flow*, McGraw-Hill Book Co., New York, N.Y., 1980.
- [3] Chen, H.C. and Patel, V.C., "Near-Wall Turbulence Models for Complex Flows Including Separation," *AIAA Journal*, Vol. 26, No. 6, 1988, pp. 641-648.
- [4] Chen, H.C., "Assesment of a Reynolds Stress Closure Model for Appendage-Hull Junction Flows," *Journal of Fluids Engineering*, Vol. 117, No. 4, 1995, pp. 557-563.
- [5] Chen, H.C., "Submarine Flows Studied by Second-Moment Closure," *Journal of Engineering Mechanics*, Vol. 121, No. 10, 1995, pp. 1136-1146.
- [6] Speziale, C.G., Sarkar, S., and Gatski, T.B., "Modeling of the Pressure-Strain Correlation of Turbulence: An Invariant Dynamical Systems Approach," *Journal of Fluid Mechanics*, Vol. 227, 1991, pp. 245-272.
- [7] Daly, B.J. and Harlow, F.H., "Transport Equations in Turbulence," *The Physics of Fluids*, Vol. 13, 1970, pp. 2634-2649.

- [8] Shima, N., "A Reynolds-Stress Model for Near-Wall and Low-Reynolds-Number Regions," *Journal of Fluids Engineering*, Vol. 10, 1988, pp. 38-44.
- [9] Chen, H.C., Patel, V.C., and Ju, S., "Solutions of Reynolds-Averaged Navier-Stokes Equations for Three-Dimensional Incompressible Flows," *Journal of Computational Physics*, Vol. 88, No. 2, 1990, pp. 305-336.
- [10] Launder, B.E., "Second-Moment Closure: Present ... and Future?" *International Journal of Heat and and Fluid Flow*, Vol. 10, No. 4, 1989, pp. 282-300.
- [11] Eggels, J.G.M. et. al., "Fully developed turbulent pipe flow: a comparison between direct numerical simulation and experiment," *Journal of Fluid Mechanics*, Vol. 268, 1994. pp. 175-209.
- [12] Lytle, D. and Webb, B., "Air jet impingement heat transfer at low nozzle-plate spacings," *International Journal of Heat and Mass Transfer*, Vol. 37, 1994, pp. 1687-1697.
- [13] Behnia, M., Parneix, S., and Durbin P.A., "Prediction of heat transfer in an axisymmetric turbulent jet impinging on a flat plate," *International Journal of Heat and Mass Transfer*, Vol. 41, No. 12, 1998, pp. 1845-1855.
- [14] Bunker, R.S. and Metzger, D.E., "Local Heat Transfer in Internally Cooled Turbine Airfoil Leading Edge Regions: Part One - Impingement Cooling Without Film Coolant Extraction," *Journal of Turbomachinery*, Vol. 112, 1990, pp. 451-458.
- [15] Fitzgerald, J.A. and Garinella S.V., "A study of the flow field of a confined and submerged impinging jet," *International Journal of Heat and Mass Transfer*, Vol. 41, 1998, pp. 1025-1034.

Appendix A

Derivation of the RANS equations

Let us start from the instantaneous momentum equation, where the instantaneous contravariant velocity component in the i th direction is given by V^{*i} .

$$\frac{\partial V^{*i}}{\partial t} + V^{*j}V_j^{*i} = F^{*i} - \frac{1}{\rho}g^{ij}p_{,j} + \nu g^{jk}V_{,jk}^{*i} \quad (\text{A.1})$$

We now proceed to split the instantaneous velocity component, V^{*i} , into its mean and fluctuating components:

$$V^{*i} = V^i + v^i \quad (\text{A.2})$$

Thus, the instantaneous mean momentum equation becomes:

$$\frac{\partial(V^i + v^i)}{\partial t} + (V^j + v^j)(V^i + v^i)_{,j} = (F^i + f^i) - \frac{1}{\rho}g^{ij}(p + p')_{,j} + \nu g^{jk}(V^i + v^i)_{,jk} \quad (\text{A.3})$$

The next step is to take the ensemble average of (A.3):

$$\frac{\partial(\overline{V^i + v^i})}{\partial t} + \overline{(V^j + v^j)(V^i + v^i)}_{,j} = \overline{(F^i + f^i)} - \frac{1}{\rho} g^{ij} \overline{(p + p')}_{,j} + \nu g^{jk} \overline{(V^i + v^i)}_{,jk} \quad (\text{A.4})$$

Knowing that the ensemble average of a fluctuating quantity is identically equal to zero, i.e. $\overline{v^j} = 0$, equation (A.4) reduces to the ensembled averaged momentum equation or the Reynolds Averaged Navier-Stokes (RANS) equation:

$$\frac{\partial V^i}{\partial t} + V^j V_{,j}^i + \overline{v^j v_j^i} = F^i - \frac{1}{\rho} g^{ij} p_{,j} + \nu g^{jk} V_{,jk}^i \quad (\text{A.5})$$

Appendix B

Derivation of the Reynolds Stress Tensor Transport equation

Next, we subtract the instantaneous momentum equation (A.3) from the averaged momentum equation (A.5) to obtain the fluctuating momentum equation:

$$\frac{\partial v^i}{\partial t} + V^j v^i_{,j} + v^j V^i_{,j} + v^j v^i_{,j} - \overline{v^j v^i_{,j}} = f^i - \frac{1}{\rho} g^{ij} p'_{,j} + \nu g^{jk} v^i_{,jk} \quad (\text{B.1})$$

Or equivalently

$$\frac{\partial v^i}{\partial t} + V^m v^i_{,m} + v^m V^i_{,m} + v^m v^i_{,m} - \overline{v^m v^i_{,m}} = f^i - \frac{1}{\rho} g^{im} p'_{,m} + \nu g^{mn} v^i_{,mn} \quad (\text{B.2})$$

Let us now denote the above equation by m^i and multiply it by v^j and add its symmetric component:

$$v^j m^i + v^i m^j \quad (\text{B.3})$$

The resulting expression is rather complicated, so let us analyze term by term:

- TERM 1:

$$v^j \frac{\partial v^i}{\partial t} + v^i \frac{\partial v^j}{\partial t} = \frac{\partial(v^i v^j)}{\partial t}$$

- TERM 2:

$$V^m (v^j v^i_{,m} + v^i v^j_{,m}) = V^m (v^i v^j)_{,m}$$

- TERM 3:

$$v^m v^j V^i_{,m} + v^m v^i V^j_{,m}$$

- TERM 4:

$$v^m v^j v^i_{,m} + v^m v^i v^j_{,m} = (v^m v^i v^j)_{,m}$$

- TERM 5:

$$v^j \overline{v^m v^i_{,m}} + v^i \overline{v^m v^j_{,m}}$$

- TERM 6:

$$v^j f^i + v^i f^j$$

- TERM 7:

$$\frac{1}{\rho} g^{im} v^j p'_{,m} + \frac{1}{\rho} g^{jm} v^i p'_{,m} = \frac{1}{\rho} g^{im} (v^j p')_{,m} + \frac{1}{\rho} g^{jm} (v^i p')_{,m} - \frac{1}{\rho} g^{im} v^j_{,m} p' - \frac{1}{\rho} g^{jm} v^i_{,m} p'$$

- TERM 8:

$$\nu g^{mn} v^j v^i_{,mn} + \nu g^{mn} v^i v^j_{,mn} = \nu g^{mn} (v^j v^i_{,mn} + v^i v^j_{,mn})$$

Note that $(v^i v^j)_{,mn} = (v^j v^i_{,mn} + v^i v^j_{,mn}) + v^i_{,m} v^j_{,n} + v^j_{,m} v^i_{,n}$, thus TERM 8 simplifies to:

$$\nu g^{mn} (v^i v^j)_{,mn} - 2\nu g^{mn} v^i_{,m} v^j_{,n}$$

Putting all the pieces together yields the following expression:

$$\begin{aligned}
\frac{\partial(\overline{v^i v^j})}{\partial t} + V^m (\overline{v^i v^j})_{,m} &= -(\overline{v^m v^j V_{,m}^i} + \overline{v^m v^i V_{,m}^j}) - (\overline{v^m v^i v^j})_{,m} + \overline{v^j \overline{v^m v^i}} \\
&+ \overline{v^i \overline{v^m v^j}} + \overline{v^j f^i} + \overline{v^i f^j} - \frac{1}{\rho} g^{im} (\overline{v^j p'})_{,m} - \frac{1}{\rho} g^{jm} (\overline{v^i p'})_{,m} + \frac{1}{\rho} g^{im} \overline{v_{,m}^j p'} \\
&+ \frac{1}{\rho} g^{jm} \overline{v_{,m}^i p'} + \nu g^{mn} (\overline{v^i v^j})_{,mn} - 2\nu g^{mn} \overline{v_{,m}^i v_{,n}^j}
\end{aligned} \tag{B.4}$$

The next step is to take the ensemble average (which eliminates two of the terms) and join like terms (namely, the fluctuating pressure terms):

$$\begin{aligned}
\frac{\partial(\overline{v^i v^j})}{\partial t} + V^m (\overline{v^i v^j})_{,m} &= -(\overline{v^m v^j V_{,m}^i} + \overline{v^m v^i V_{,m}^j}) - (\overline{v^m v^i v^j})_{,m} \\
&+ \overline{v^j f^i} + \overline{v^i f^j} - \frac{1}{\rho} g^{im} (\overline{v^j p'})_{,m} - \frac{1}{\rho} g^{jm} (\overline{v^i p'})_{,m} + \frac{\overline{p'}}{\rho} (g^{im} \overline{v_{,m}^j} + g^{jm} \overline{v_{,m}^i}) \\
&+ \nu g^{mn} (\overline{v^i v^j})_{,mn} - 2\nu g^{mn} \overline{v_{,m}^i v_{,n}^j}
\end{aligned} \tag{B.5}$$

Let $\overline{v^i v^j} = R^{ij}$, thus the Reynolds Stress Tensor Transport equation takes its "almost" final form:

$$\begin{aligned}
\frac{\partial R^{ij}}{\partial t} + V^m R_{,m}^{ij} &= -(R^{im} V_{,m}^j + R^{jm} V_{,m}^i) - (\overline{v^m v^i v^j})_{,m} \\
&+ \overline{v^j f^i} + \overline{v^i f^j} - \frac{1}{\rho} g^{im} (\overline{v^j p'})_{,m} - \frac{1}{\rho} g^{jm} (\overline{v^i p'})_{,m} + \frac{\overline{p'}}{\rho} (g^{im} \overline{v_{,m}^j} + g^{jm} \overline{v_{,m}^i}) \\
&+ \nu g^{mn} R_{,mn}^{ij} - 2\nu g^{mn} \overline{v_{,m}^i v_{,n}^j}
\end{aligned} \tag{B.6}$$

Attaching physical significance to each term yields the final form of the Reynolds Stress Tensor Transport equation:

$$\boxed{\frac{\partial R^{ij}}{\partial t} + C^{ij} = P^{ij} + D_v^{ij} + F^{ij} + D_p^{ij} + \Phi^{ij} + D_v'^{ij} - \epsilon^{ij}} \tag{B.7}$$

Where

- C^{ij} : Convection

$$V^m R_{,m}^{ij}$$

- P^{ij} : Production

$$-(R^{im}V_{,m}^j + R^{jm}V_{,m}^i)$$

- D_{ϕ}^{ij} : Diffusion by Velocity Fluctuation

$$-(\overline{v^m v^i v^j})_{,m}$$

- F^{ij} : Force Field

$$\overline{v^j f^i} + \overline{v^i f^j}$$

- D_p^{ij} : Diffusion by Pressure Fluctuation

$$-\frac{1}{\rho}g^{im}(\overline{v^j p'})_{,m} - \frac{1}{\rho}g^{jm}(\overline{v^i p'})_{,m}$$

- Φ^{ij} : Pressure-Strain

$$\frac{\overline{p'}}{\rho}(g^{im}\overline{v_{,m}^j} + g^{jm}\overline{v_{,m}^i})$$

- D_{ν}^{ij} : Viscous Diffusion

$$\nu g^{mn} R_{,mn}^{ij}$$

- ϵ^{ij} : Viscous Dissipation

$$2\nu g^{mn}\overline{v_{,m}^i v_{,n}^j}$$

Biographical Sketch

Juan Pablo Pontaza was born on July 31, 1976, in Guatemala City, Guatemala. He received his elementary education in Guatemala City, Guatemala and part of his secondary education in Altensteig, Germany. He enrolled in Texas A&M University in January of 1995, majoring in Mechanical Engineering. While attending Texas A&M he participated in the University Honors Program, the University Undergraduate Research Fellows, and the Engineering Scholars Program. He will graduate in May 1999 and will continue with his graduate studies at the Massachusetts Institute of Technology in the department of Aeronautics and Astronautics.